Composites Part B 131 (2017) 260–281

Contents lists available at ScienceDirect

Composites Part B

journal homepage: www.elsevier.com/locate/compositesb

# Diameter-dependent elastic properties of carbon nanotube-polymer composites: Emergence of size effects from atomistic-scale simulations

M. Malagù [a, b], M. Goudarzi [a], A. Lyulin [c], E. Benvenuti [b, *], A. Simone [a]

[a] Faculty of Civil Engineering and Geosciences, Delft University of Technology, P.O. Box 5048, 2600 GA Delft, The Netherlands
[b] Department of Engineering, University of Ferrara, Via Saragat 1, 44122 Ferrara, Italy
[c] Department of Applied Physics, Eindhoven University of Technology, P.O. Box 513, 5600 MB Eindhoven, The Netherlands

ARTICLE INFO

*Article history:*
Received 22 December 2016
Received in revised form
16 May 2017
Accepted 25 July 2017
Available online 4 August 2017

*Keywords:*
Polymer-matrix composites (PMCs)
Interface/interphase
Atomistic simulations
Finite element analysis (FEA)

ABSTRACT

We propose a computational procedure to assess size effects in nonfunctionalized single-walled carbon nanotube (CNT)-polymer composites. The procedure upscales results obtained with atomistic simulations on a composite unit cell with one CNT to an equivalent continuum composite model with a large number of CNTs. Molecular dynamics simulations demonstrate the formation of an ordered layer of polymer matrix surrounding the nanotube. This layer, known as the interphase, plays a central role in the overall mechanical response of the composite. Due to poor load transfer from the matrix to the CNT, the reinforcement effect attributed to the CNT is negligible; hence the interphase is regarded as the only reinforcement phase in the composite. Consequently, the mechanical properties of the interface and the CNT are not derived since their contribution to the elastic response of the composite is negligible. To derive the elastic properties of the interphase, we employ an intermediate continuum micromechanical model consisting of only the polymer matrix and a three-dimensional fiber representing the interphase. The Young's modulus and Poisson's ratio of the equivalent fiber, and therefore of the interphase, are identified through an optimization procedure based on the comparison between results from atomistic simulations and those obtained from an isogeometric analysis of the intermediate micromechanical model. Finally, the embedded reinforcement method is employed to determine the macroscopic elastic properties of a representative volume element of a composite with various fiber volume fractions and distributions. We then investigate the role of the CNT diameter on the elastic response of a CNT-polymer composite; our simulations predict a size effect on the composite elastic properties, clearly related to the interphase volume fraction.



## 1. Introduction

The diameter of carbon nanotubes (CNTs) can induce size effects in the structural and mechanical properties of CNT-polymer composites [1–7]. Due to the high aspect ratio of CNTs, these size effects can only be assessed using computational multiscale procedures. To this end, we present a computational procedure to upscale nanoscale information, obtained with atomistic simulations, to a continuum micromechanical model at the composite scale for the analysis of the size-dependent elastic properties of a non-functionalized single-walled CNT-polymer composite. In the following, the term “continuum” indicates a volume where a continuous distribution of material replaces the atomistic structure.

Diameter-induced effects were first noticed by means of pull-out tests that showed a decrease of the interfacial shear strength between a CNT and the polymer matrix around it with increasing nanotube diameter [2,6]. Although a limited number of experimental results is available [2,6], the observed trend for the interfacial shear strength has been confirmed by means of atomistic simulations [3,5,8]. This size effect was attributed to the increasing number of non-bonded interactions between polymer and CNT atoms with decreasing nanotube diameter [4]. It is however

* Corresponding author.
*E-mail addresses:* m.malagu@tudelft.nl (M. Malagù), m.goudarzi@tudelft.nl (M. Goudarzi), a.v.lyulin@tue.nl (A. Lyulin), bnvlne@unife.it (E. Benvenuti), a.simone@tudelft.nl (A. Simone).

http://dx.doi.org/10.1016/j.compositesb.2017.07.029

recognized that another phase in CNT-polymer composites contributes to the overall mechanical response beside the CNT-polymer interface.

Several works (see Refs. [9,10] for an extensive review) indicate that the formation of an ordered layer of polymer matrix around a nanotube is relevant for the enhancement of the mechanical properties of the composite. Such a layer, usually referred to as the interphase, has been identified in a wide class of CNT-polymer composites [9]. In particular, Coleman and coworkers [11,12] suggested that the reinforcement observed in CNT-polyvinyl alcohol composites was mainly provided by the interphase while the load transfer from the matrix to the CNT was poor. Similar results, emphasizing the reinforcement effect of the interphase and the soft interface in nonfunctionalized CNT-polymer composites have been experimentally observed with various polymer matrices [13–18].

The characterization of the interphase is usually performed with computer simulations since they enable a detailed analysis of the polymer chain structure. Using molecular dynamics (MD) simulations, Falkovich et al. [19] showed that the ordering of the interphase in CNT-polyimide composites increases with the nanotube diameter. Similar results were also achieved with a generic amorphous polymer model [20]. The mechanical properties of the interphase are typically assessed through a continuum model that is mechanically equivalent to an atomistic reference model [21–24]. In an alternative approach, proposed by Choi et al. [7], the stiffness of the interphase in CNT-epoxy composites is studied through a reverse engineering procedure by comparing the elastic response of the MD system with that of an intermediate continuum micromechanical model. Results showed that the interphase stiffness increases by decreasing the CNT diameter. However, their atomistic model considered periodic infinitely long nanotubes. Consequently, once the simulation cell is loaded in tension along the CNT axis direction, matrix and nanotube are equally stretched while in reality the CNT should deform according to the stresses transferred to it from the matrix through the interface.

The multiscale procedure employed in this contribution for the characterization of size effects in the elastic properties of the CNT-polymer composites is summarized in Fig. 1. As proposed in previous works [7,21,22,24], we employed (a) atomistic simulations to investigate structural and mechanical features of CNT-polymer composites at the nanoscale, (b) an intermediate continuum micromechanical model to estimate the mechanical properties of the reinforcement phase (i.e., the Young's modulus and Poisson's ratio of the interphase region), and (c) a continuum micromechanical model to asses the macroscopic elastic moduli of the composite.

As shown in Fig. 1a, the atomistic models consider a short uncapped nonfunctionalized single-walled CNT of finite length fully embedded into the simulation box. This setup enables load transfer from a coarse-grained amorphous monodisperse polyethylene-like polymer matrix [20] to the nanotube. Rather than characterizing size effects for a specific composite, we aim to explore the influence of the CNT diameter for a wider range of polymer matrices using a simple yet representative model for the polymer chains. CNT-polymer composites with nanotubes of different diameter are generated in the molecular dynamics setting described in Section 2.1. The equilibrated configurations are examined in Section 2.2 to characterize the geometry of CNT, interface, interphase and bulk polymer matrix. The roles of these four phases in the elastic response of the composite are explored through uniaxial tensile tests performed with molecular mechanics (MM) in Section 2.3. At the same time, MM uniaxial tensile tests are also performed on a pure polymer matrix to calculate the elastic properties of the polymer. As discussed in Section 2.4, and observed in the literature [11–18] for real CNT-polymer composites, the interphase is the true reinforcement phase in the composite while the effect of the embedded CNT on the elastic response of the composite is negligible.

To take into account the effect of the interphase in a computationally feasible manner at the composite level with a realistic number of CNTs, we have defined an equivalent fiber. The approach consists in the definition of an intermediate continuum

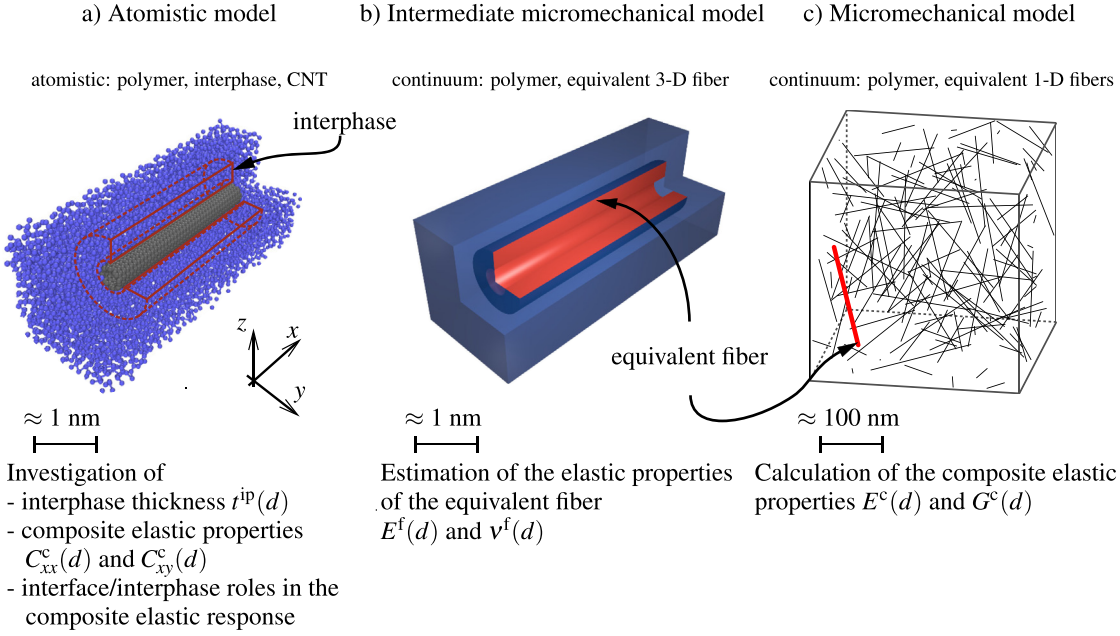


**Fig. 1.** Objectives of the multiscale procedure for the characterization of size effects induced by the nanotube diameter $d$ on the CNT-polymer composite elastic properties. In the intermediate micromechanical model and the micromechanical model, only the bulk polymer matrix and the interphase have been considered since the contributions of the nanotube and the interface on the elastic response of the composite are negligible.

micromechanical model that, as shown in Fig. 1b, contains the bulk polymer and a three-dimensional domain referred to as equivalent fiber to model the interphase. Due to the soft interface, both the interface and the CNT are not considered in the intermediate micromechanical model and their elastic properties are not investigated. The geometry of the equivalent fiber coincides with that of the interphase derived in Section 2.2 in the atomistic model. Its Young's modulus and Poisson's ratio are determined through a parameter estimation procedure by comparing the mechanical responses of the one-fiber composite obtained with the atomistic model and the intermediate micromechanical model in Section 3. In particular, isogeometric analysis is employed to obtain the mechanical response of the micromechanical continuum model as detailed in Section 3.1.

With the interphase and bulk polymer mechanical properties at hand, a micromechanical analysis of the CNT-polymer composite shown in Fig. 1c is conducted. Elastic properties of several representative volume elements (RVEs) with unidirectional and randomly oriented CNTs are derived by means of FEM simulations (see Section 4) to assess diameter effects at different nanotube volume ratios. Akin to the intermediate continuum model in Fig. 1b, only the bulk polymer and equivalent continuum fibers (the interphases) are considered. Due to the high aspect ratio of real nanotubes and to their large number in an RVE, each equivalent continuum three-dimensional fiber is modeled as a one-dimensional fiber by means of the embedded reinforcement method [25] described in Section 4.1. The results of the FEM analyses are finally compared with those obtained with classical micromechanical models in Section 5.

The proposed computational procedure is not only intended for the assessment of size effects. It also provides a strategy to understand the role played by the different phases in the composite, a relevant question about CNT-polymer composites and other nanocomposite materials [26,27]. Despite the approximations of the polymer model at the atomistic level, the results of our simulations are qualitatively comparable with literature findings using real polymers as discussed in Section 6.

The standard notation $(n, m)$ to describe single-walled CNTs [28] is adopted throughout the paper. Moreover, the notation $(n, m)$-polymer is used to denote a polymer matrix reinforced with $(n, m)$ single-walled CNTs.

## 2. Atomistic modeling of CNT-polymer composites

Atomistic simulations of representative CNT-polymer composites are performed to characterize the nanoscale features required to establish the intermediate continuum model in Section 3. To this end, four composites embedding uncapped nanotubes of different diameter are generated through MD simulations as detailed in Section 2.1. Here, we considered CNT-polymer composites with the same nanotube volume fraction to explore the effects induced by the CNT diameter. In particular, the effect on the interphase volume fraction and the elastic properties of the CNT-polymer composites are investigated (see Sections 2.2 and 2.3, respectively). Furthermore, based on the results obtained from MM uniaxial tensile tests, the roles of the CNT and the interphase in the mechanical response of the composite are discussed in Section 2.4.

### 2.1. Method

The atomistic model for the CNT-polymer composite is identical to that used in Reference [20]. Fully-atomistic uncapped non-functionalized single-walled CNTs are modeled with the modified Morse potential [29–31] while the amorphous monodisperse polyethylene-like polymer is modeled with the coarse-grained Finite Extensible Nonlinear Elastic (FENE) potential [32]. This allows for the analysis of CNT diameter-induced effects as well. Polymer chemistry-specific effects are therefore avoided to explore the influence of the nanotube in a wide range of single-walled CNT-polymer composite as previously proposed in References [20,33].

The use of the modified Morse potential was motivated by its effectiveness in the analysis of fully-atomistic CNTs with molecular dynamics, molecular mechanics and molecular structural mechanics simulations as demonstrated by Belytschko et al. [29] and more recently by Malagù et al. [20,31]. Moreover, in small deformation studies as those considered in this paper, the mechanical response of CNTs predicted with the modified Morse potential is closely comparable to that obtained with the widely used, and more computationally demanding, second-generation reactive empirical bond order (REBO) potential [34].

The polymer matrix is modeled as a coarse-grained amorphous monodisperse polyethylene-like system. Each polymer chain is defined by 300 identical monomeric units (referred to as beads) covalently bonded through the FENE interatomic potential

$$U(r) = -0.5KR_0^2 \ln\left[1 - \left(\frac{r}{R_0}\right)^2\right] + 4\varepsilon_p\left[\left(\frac{\sigma_p}{r}\right)^{12} - \left(\frac{\sigma_p}{r}\right)^{6} + \frac{1}{4}\right], \quad (1)$$

where $r$ is the distance between two beads. The constants $K$ and $R_0$ are the stiffness and the maximum elongation of the polymer bonds, while $\varepsilon_p$ and $\sigma_p$ are the beads characteristic length and energy constants. According to 32, for a monodisperse polyethylene-like polymer model system, $\varepsilon_p = 5.1$ Å, $\sigma_p = 0.8903$ kcal/mol, $K = 30\sigma_p/\varepsilon_p^2$ and $R = 1.5\sigma_p$. The model employed for the nanotubes is detailed in Ref. [29]. Between polymer beads and CNT atoms only non-bonded Lennard-Jones interactions defined by the potential

$$U(r) = 4\varepsilon_{pc}\left[\left(\frac{\sigma_{pc}}{r}\right)^{12} - \left(\frac{\sigma_{pc}}{r}\right)^{6} + \frac{1}{4}\right] \quad (2)$$

are allowed. The constants $\varepsilon_{pc}$ and $\sigma_{pc}$ are calculated with the Lorentz-Berthelot rules

$$\sigma_{pc} = \frac{1}{2}(\sigma_p + \sigma_c) \quad \text{and} \quad \varepsilon_{pc} = \sqrt{\varepsilon_p \varepsilon_c}, \quad (3)$$

where $\sigma_c$ and $\varepsilon_c$ are the Lennard-Jones constants for single-walled CNT carbon atoms [35].

To explore diameter effects in CNT-polymer composites with the same nanotube volume fraction $v^{CNT}$, four different nanocomposites with $v^{CNT} \approx 0.6\%$ but with nanotubes of different diameter were generated. Since the variation of carbon nanotube weight fraction in the generated CNT-polymer composites is small [20], we can assume that the trend for the mechanical properties observed in the next sections is mainly caused by the changes in the nanotube diameter. Effects induced by the nanotube chirality are not investigated because assumed to be negligible: as observed by Ref. [20], chirality does not influence the atomic structure at the CNT-polymer interphase that determines the mechanical properties of the composite (later explained in Section 3.2). Here, only armchair ((6,6), (8,8), (10,10) and (12,12)) single-walled CNTs are considered. As shown Fig. 2a, the nanotubes, centered at $x = 0$ Å, are aligned along the $x$-axis. The length of the simulation box in the $x$-direction ($L_x \approx 180$ Å) is larger than that of the nanotubes ($l \approx 100$ Å). This allows for the assessment of the interface properties and the load transfer mechanism between polymer matrix and CNT. The dimension of the unit cell in the $y$- and $z$-direction ($L_y$ and $L_z$, respectively) is such that the interphase region is completely embedded in the simulation box, hence to avoid any

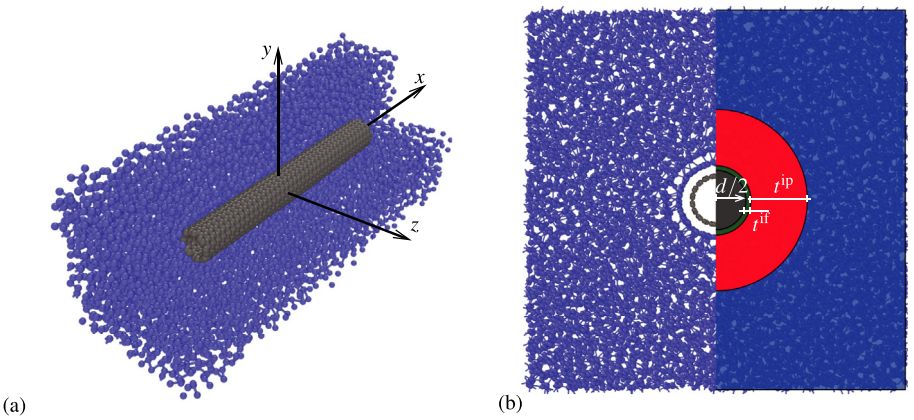


**Fig. 2.** (a) Snapshot of the atomistic model of an (8,8)-polymer composite (monomer beads in blue, single-walled CNT carbon atoms in gray). Part of the polymer matrix has been removed to reveal the embedded nanotubes. (b) Cross sectional view of the (8,8)-polymer composite. On the right half of the image, colored regions denote the composite phases: CNT (gray), interface (green), interphase (red) and bulk matrix (blue). These figures have been adapted from Reference [20]. (For interpretation of the references to colour in this figure legend, the reader is referred to the web version of this article.)

contact or intersection of the interphase with its periodic image. To fully assess the nanotube reinforcement effects, a pure polymer matrix was also generated.

Seeking for the elastic properties under quasi-static deformation through molecular mechanics (MM), CNT-polymer composite and pure polymer matrix systems are investigated in glassy state where the vibrational part of the free energy is negligible [36,37]. Therefore, all simulations have been performed on atomistic configurations below the glass transition temperature ($T_g \approx 200$ K [20]), specifically at 100 K. For each system, three different initial configurations were generated and the corresponding results were averaged. The Large-scale Atomic/Molecular Massively Parallel Simulator (LAMMPS) software package was used [38]. Newton's equations of motion were integrated with the velocity Verlet algorithm using a time step of 1 fs. The Nosé-Hoover thermostat and barostat were used. Energy minimization was performed with the conjugate gradient method. In all simulations, periodic boundary conditions in the three directions were applied. LAMMPS input scripts to generate the results discussed in the next sections are available for download at the authors' web-page.

### 2.2. Single-walled CNT and interphase volume fractions

In this section, the geometry of the phases in the CNT-polymer composite, required for the development of the intermediate continuum micromechanical model in Section 3, is determined. The corresponding volume fractions are also provided since they play a significant role in the macroscopic elastic properties discussed in Section 4.

Fig. 2b shows the cross section of an (8,8)-polymer composite and highlights the different phases characterizing single-walled CNT-polymer composites. Visual examination reveals four distinct regions. The first (in gray), with a cylindrical shape, represents the effective nanotube volume, also indicated as the effective reinforcement according to the model proposed by Pipes et al [39, Fig. 2]. and adopted by many others [40–42]. Here, the nanotube and the empty region inside it are replaced by an effective solid cylinder. A nanotube is therefore considered as a solid beam of length $l$ and circular cross section of diameter $d$ with volume

$$V^{CNT} = \pi \frac{d^2}{4} l. \tag{4}$$

The diameter of the effective reinforcement related to an $(n, m)$ single walled CNT is given in Reference [39]:

$$d = \frac{a_{cc}\sqrt{3(n^2 + m^2 + nm)}}{\pi} + t, \tag{5}$$

where $a_{cc} = 1.421$ Å is the carbon-carbon bond length and $t = 3.42$ Å is the separation distance of graphene sheets [43].

The second region (in green) is the interface. Its thickness $t^{if}$ is defined as the average equilibrium distance between the CNT surface and the first layer of polymer atoms [39]. The thickness $t^{if}$ can be determined from the analysis of the radial density profile $\rho(r)$, where $r$ is the distance from the nanotube surface (i.e., at $t/2$ from the CNT atoms), obtained from atomistic simulations. Here, $t^{if}$ has been assumed as the distance between the CNT surface ($r = 0$ Å) and the first peak in $\rho(r)$. As illustrated in Fig. 3a, the interface thickness, insensitive to the nanotube diameter, is approximately equal to 4.5 Å. This estimate is in line with literature results obtained from MD models of CNTs embedded in real polymers [5,44–46]. Analogously, examination of the density profile along the axis of the CNT (i.e. in the $x$-direction) provides the length of the interface. As shown in Fig. 3b, the peaks in $\rho(r)$ quickly decay after the end of the nanotube (i.e. at $|x| \geq l/2$), and the interface length is assumed equal to that of the nanotube. Thus, the interface volume is calculated as

$$V^{if} = \pi \frac{\left(d + 2t^{if}\right)^2 - d^2}{4} l. \tag{6}$$

The third region (in red) consists of the ordered layer of polymer matrix surrounding the nanotube, the interphase. Its thickness and length are derived by comparing the density profile in the CNT-polymer composite with that of the pure polymer matrix as previously done for real CNT-polymer composites in Refs. [23,47]. Due to statistical noise in $\rho(r)$, it is difficult to provide a precise estimate of the interphase thickness $t^{ip}$. Nevertheless, as depicted in Fig. 3a, for $r \geq 30.0$ Å the oscillations in the density profiles for all CNT-polymer composites resemble those in the pure polymer matrix. Therefore, $t^{ip}$ has been assumed 25.5 Å irrespective of the nanotube diameter. The independence of the interphase thickness from the size of the inclusion was observed in atomistic models of CNTs embedded in real polymers [19,37] and other nanocomposite systems [48,49]. It is however worth mentioning that $t^{ip}$ shows a temperature dependence as shown in [20, Fig. 6]; in this work $t^{ip}$

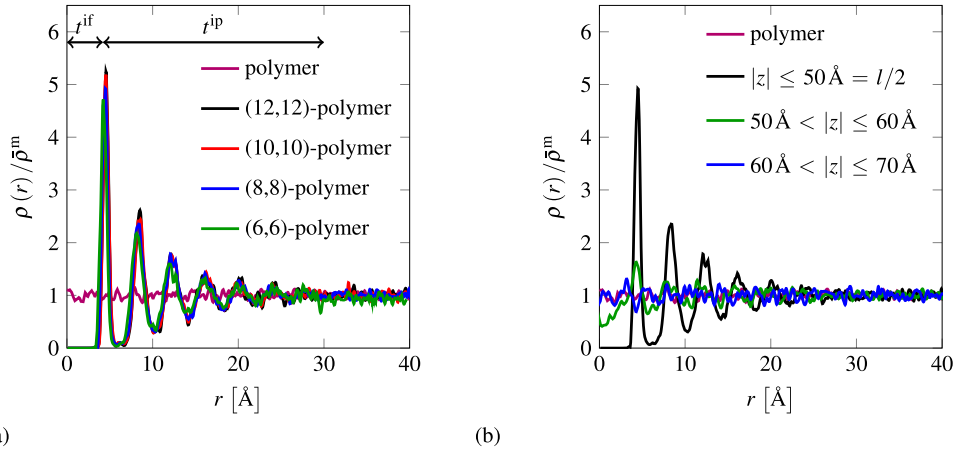


**Fig. 3.** (a) Density profile in the polymer matrix and in (*n*,*n*)-polymer composites at 100 K as a function of the distance *r* from the nanotube surface. All curves have been normalized with respect to the average density of the polymer matrix $\bar{\rho}^m = 0.818$ g/cm$^3$ (this figure is adapted from Reference [20]). (b) Density profile in the polymer matrix and in an (8,8)-polymer composites evaluated at different position along the longitudinal axis of the nanotube (i.e. *x*-axis).

has been estimated at $T = 100$ K. Fig. 3b shows that the interphase length can be set equal to $l$, thus yielding the interphase volume

$$V^{ip} = \pi \frac{\left(d + 2t^{if} + 2t^{ip}\right)^2 - \left(d + 2t^{if}\right)^2}{4} l. \tag{7}$$

Fig. 3a shows that nanotubes with bigger diameter lead to highest peaks in the interphase density profile. As thoroughly discussed in Refs. [19,20], this indicates that the ordering of the interphase atomic structure increases with the diameter of the embedded CNT.

Finally, the fourth region (in blue) corresponds to the amorphous bulk polymer whose structure is not affected by the CNT. Knowing the volume of the MD unit cell $V^{cell}$ (the dimensions of the CNT-polymer composite unit cell at this temperature are in Table 1), the volume of amorphous polymer is

$$V^{bulk} = V^{cell} - \left(V^{CNT} + V^{if} + V^{ip}\right). \tag{8}$$

From the volume of the aforementioned regions, the corresponding volume fractions are easily calculated dividing (4)–(8) by $V^{cell}$. For the particular case of the nanotube and the interphase volume fractions we have

$$\upsilon^{CNT} = \frac{V^{CNT}}{V^{cell}} = \pi \frac{d^2 l}{4V^{cell}} \tag{9}$$

and

$$\upsilon^{ip} = \frac{V^{ip}}{V^{cell}} = \upsilon^{CNT} \frac{V^{ip}}{V^{CNT}} = \upsilon^{CNT} \frac{\left(4t^{ip}\right)^2 + 4dt^{ip} + 8t^{ip}t^{if}}{d^2}, \tag{10}$$

respectively. As a direct consequence, Fig. 4 shows that when composites with the same CNT volume fraction $\upsilon^{CNT}$ but different CNT diameter are considered, the volume fraction of the interphase

**Table 1**
Dimensions of the (*n*,*n*)-polymer composites at 100 K.

| Composite | $d$ [Å] | $L_x$ [Å] | $L_y$ [Å] | $L_z$ [Å] |
|---|---|---|---|---|
| (6,6)-polymer | 8.14 | 66.9 | 66.9 | 181.2 |
| (8,8)-polymer | 10.86 | 91.9 | 91.9 | 175.9 |
| (10,10)-polymer | 13.57 | 114.7 | 114.7 | 177.9 |
| (12,12)-polymer | 16.28 | 136.3 | 136.3 | 181.7 |

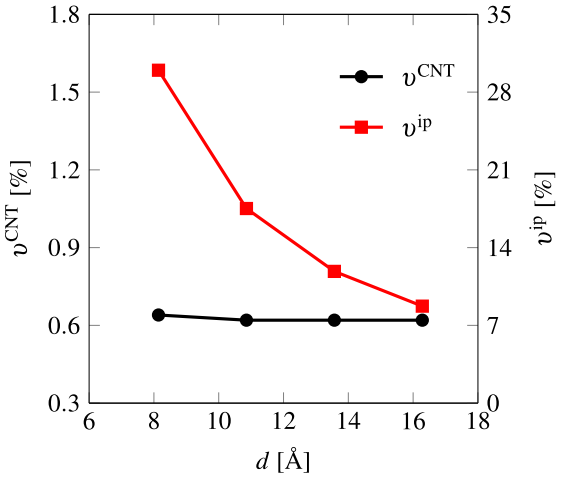


**Fig. 4.** CNT volume fraction $\upsilon^{CNT}$ and interphase volume fraction $\upsilon^{ip}$ calculated with (9) and (7), respectively, for four different (*n*,*n*)-polymer composites.

$\upsilon^{ip}$ decreases with increasing $d$. This result has a considerable impact on the composite mechanical properties discussed in Section 5. Moreover, as indicated in eq. (10), $\upsilon^{ip}$ increases linearly with the CNT volume fraction as observed experimentally 11.

### 2.3. Uniaxial tensile test simulations

Mechanical properties of CNT-polymer composites under uniaxial quasi-static loading are determined with MM simulations. After each strain increment, consisting in a small uniaxial deformation applied in the direction of the nanotube axis (i.e., the *x* axis), the total potential energy of the system is minimized. More specifically, making use of the Voigt notation, the strain increment defined by the macrostrain tensor

$$\bar{\boldsymbol{\varepsilon}} = [\bar{\varepsilon}_{xx} \;\; 0 \;\; 0 \;\; 0 \;\; 0 \;\; 0]^T = [0.01\% \;\; 0 \;\; 0 \;\; 0 \;\; 0 \;\; 0]^T, \tag{11}$$

with the superscript T denoting transpose, is applied to the periodic unit cell (in (11) and throughout this work a bar above a symbol indicates a macroscopic quantity). Afterwards, the total potential energy of the system is minimized keeping the size of the box fixed [50–52]. This procedure is repeated until the total axial strain is

equal to 5% since MM simulations on glassy polymers can be performed only under small deformation since the adopted interatomic potentials are not suitable to model the nonlinear response of the material.

The first significant insight concerning the deformation mechanism in CNT-polymer composite is provided by the analysis of the strain energy contributions during deformation. Here, the total strain energy $\Pi^{\text{total}}$ is decomposed into the contribution of the CNT ($\Pi^{\text{CNT}}$), the interface ($\Pi^{\text{if}}$), the interphase ($\Pi^{\text{ip}}$), and the bulk ($\Pi^{\text{bulk}}$). As shown in Fig. 5a for an (8,8)-polymer composite, $\Pi^{\text{ip}}$ and $\Pi^{\text{bulk}}$ are the major contributions to $\Pi^{\text{total}}$ while $\Pi^{\text{if}}$ and $\Pi^{\text{CNT}}$ are negligible. However, since in classical short fiber composites the reinforcement efficiency and, consequently, the axial strain in the fiber increases with its length, we repeated these measurements for a composite embedding an $(8,8)$ CNT four times longer ($l = 40$ nm). Nevertheless, as shown in Fig. 5b, the corresponding results are analogous to those obtained with the shorter nanotube (see Table 2 for a comparison of the strain energy contributions at $\bar{\varepsilon}_{xx} = 5$ %). This indicates that, due to poor adhesion with the polymer matrix, negligible deformation occurs in the CNT. Thus, the mechanical response of the composite can be determined to a good approximation by just considering interphase and bulk polymer. An analogous conclusion has been reached by Coleman and coworkers [11,12] in their experiments on real CNT-polymer composites.

The results obtained from the MM uniaxial tensile tests have been used to estimate the effect of the reinforcement induced by the inclusion of a nanotube into a polymer matrix. Since the nanotubes are aligned along the $x$-direction, the generated CNT-polymer composites are transversely isotropic and the elastic constitutive relations are expressed by

$$\begin{bmatrix} \bar{\sigma}_{xx} \\ \bar{\sigma}_{yy} \\ \bar{\sigma}_{zz} \\ \bar{\sigma}_{xy} \\ \bar{\sigma}_{xz} \\ \bar{\sigma}_{yz} \end{bmatrix} = \begin{bmatrix} C^{\text{c}}_{xx} & C^{\text{c}}_{xy} & C^{\text{c}}_{xy} & 0 & 0 & 0 \\ C^{\text{c}}_{xy} & C^{\text{c}}_{yy} & C^{\text{c}}_{yz} & 0 & 0 & 0 \\ C^{\text{c}}_{xy} & C^{\text{c}}_{yz} & C^{\text{c}}_{yy} & 0 & 0 & 0 \\ 0 & 0 & 0 & 2G^{\text{c}}_{xy} & 0 & 0 \\ 0 & 0 & 0 & 0 & 2G^{\text{c}}_{xy} & 0 \\ 0 & 0 & 0 & 0 & 0 & \dfrac{C^{\text{c}}_{yy} - C^{\text{c}}_{yz}}{2} \end{bmatrix} \begin{bmatrix} \bar{\varepsilon}_{xx} \\ \bar{\varepsilon}_{yy} \\ \bar{\varepsilon}_{zz} \\ \bar{\varepsilon}_{xy} \\ \bar{\varepsilon}_{xz} \\ \bar{\varepsilon}_{yz} \end{bmatrix}, \tag{12}$$

**Table 2**
Normalized value of the strain energy contributions at $\bar{\varepsilon}_{xx} = 5$ %.

| | $\Pi^{\text{CNT}}/\Pi^{\text{total}}$ [%] | $\Pi^{\text{if}}/\Pi^{\text{total}}$ [%] | $\Pi^{\text{ip}}/\Pi^{\text{total}}$ [%] | $\Pi^{\text{bulk}}/\Pi^{\text{total}}$ [%] |
|---|---|---|---|---|
| $l = 10$nm | 1.55 | 1.40 | 24.15 | 72.60 |
| $l = 40$nm | 1.15 | 1.14 | 24.90 | 72.81 |

where $C^{\text{c}}_{ij}$ and $\bar{\sigma}_{ij}$ are the components of the elasticity tensor and the macroscopic stress tensor in matrix form, respectively. The elasticity matrix $\boldsymbol{C}^{\text{c}}$ in (12) is defined by five independent elastic constants. In this work, however, we will determine only $C^{\text{c}}_{xx}$ and $C^{\text{c}}_{xy}$ since, as shown in Section 3, the other components are not relevant for the mechanical characterization of the interphase. Substituting (11) into (12), we obtain

$$C^{\text{c}}_{xx} = \frac{\bar{\sigma}_{xx}}{\bar{\varepsilon}_{xx}} \quad \text{and} \quad C^{\text{c}}_{xy} = \frac{\bar{\sigma}_{yy}}{\bar{\varepsilon}_{xx}} = \frac{\bar{\sigma}_{zz}}{\bar{\varepsilon}_{xx}}, \tag{13}$$

where $\bar{\sigma}_{xx}$, $\bar{\sigma}_{yy}$ and $\bar{\sigma}_{zz}$ were derived from the MM simulations.

Similarly, the elastic properties were determined for the pure polymer matrix. As expected, tensile tests in all three directions yielded an isotropic response. Its stress-strain relations is expressed as

$$\begin{bmatrix} \bar{\sigma}_{xx} \\ \bar{\sigma}_{yy} \\ \bar{\sigma}_{zz} \\ \bar{\sigma}_{xy} \\ \bar{\sigma}_{xz} \\ \bar{\sigma}_{yz} \end{bmatrix} = \begin{bmatrix} C^{\text{m}}_{xx} & C^{\text{m}}_{xy} & C^{\text{m}}_{xy} & 0 & 0 & 0 \\ C^{\text{m}}_{xy} & C^{\text{m}}_{xx} & C^{\text{m}}_{xy} & 0 & 0 & 0 \\ C^{\text{m}}_{xy} & C^{\text{m}}_{xy} & C^{\text{m}}_{xy} & 0 & 0 & 0 \\ 0 & 0 & 0 & \dfrac{C^{\text{m}}_{xx} - C^{\text{m}}_{xy}}{2} & 0 & 0 \\ 0 & 0 & 0 & 0 & \dfrac{C^{\text{m}}_{xx} - C^{\text{m}}_{xy}}{2} & 0 \\ 0 & 0 & 0 & 0 & 0 & \dfrac{C^{\text{m}}_{xx} - C^{\text{m}}_{xy}}{2} \end{bmatrix} \begin{bmatrix} \bar{\varepsilon}_{xx} \\ \bar{\varepsilon}_{yy} \\ \bar{\varepsilon}_{zz} \\ \bar{\varepsilon}_{xy} \\ \bar{\varepsilon}_{xz} \\ \bar{\varepsilon}_{yz} \end{bmatrix}, \tag{14}$$

where the superscript m identifies the elastic components of the polymer matrix. In particular, $C^{\text{m}}_{xx} = 5.14$ GPa and $C^{\text{m}}_{xy} = 2.90$ GPa. As shown in Fig. 6, $C^{\text{c}}_{xx}$ is always higher than $C^{\text{m}}_{xx}$ while the opposite is observed comparing $C^{\text{c}}_{xy}$ and $C^{\text{m}}_{xy}$. Therefore, as shown in previous works on real CNT-polymer composites [7,22,37], the presence of a CNT yields higher elastic constants in the axial direction compared to those of the pure polymer matrix.

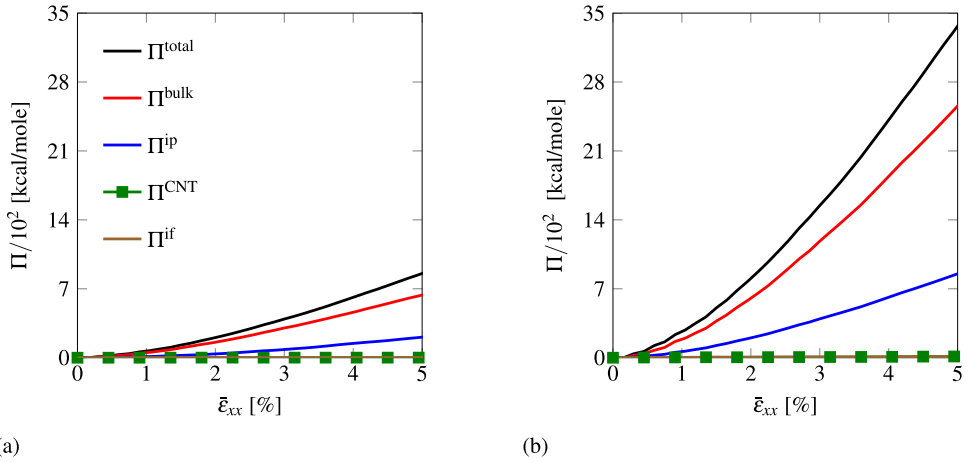


**Fig. 5.** Analysis of the total strain energy $\Pi^{\text{total}}$ and its separate contributions from CNT ($\Pi^{\text{CNT}}$), interface ($\Pi^{\text{if}}$), interphase ($\Pi^{\text{ip}}$) and bulk ($\Pi^{\text{bulk}}$) during uniaxial tension of two CNT-polymer composites with an $(8,8)$ nanotube of length (a) 10 and (b) 40 nm.

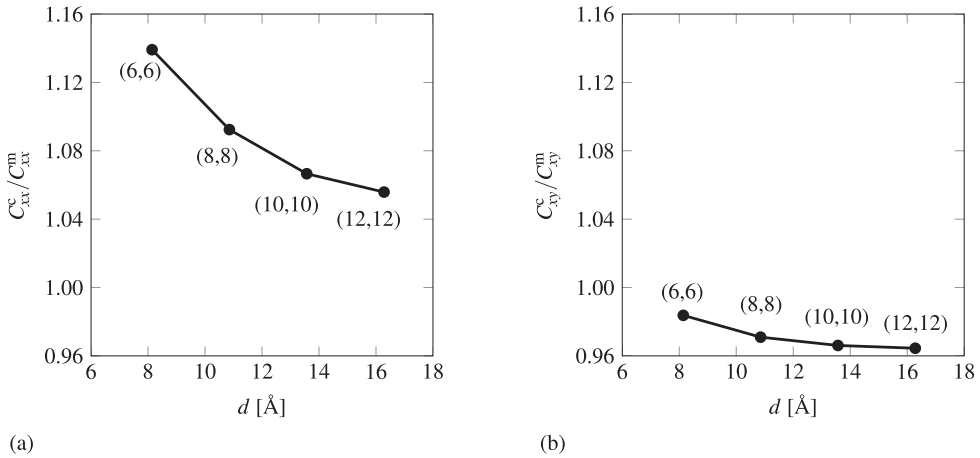


**Fig. 6.** Normalized elastic components (a) $C^c_{xx}$ and (b) $C^c_{xy}$ of four ($n$,$n$)-polymer composites. The results have been normalized with respect to the elastic components of the polymer matrix $C^m_{xx} = 5.14$ GPa and $C^m_{xy} = 2.90$ GPa.

### 2.4. Interface versus interphase

Results from MM suggested that the reinforcement in the nonfunctionalized CNT-polymer composites is merely determined by the interphase. The role of the nanotube, due to the weak atomic interactions at the interface, is limited to the nucleation of the interphase layer.

Although there is no consensus [26] about the reinforcement offered by the CNT through the interactions at the interface and the interphase, some experimental results on nonfunctionalized CNT-polymer composites support our findings. For instance, Coleman and coworkers [11,12] associated the reinforcement in CNT-polyvinyl alcohol composites to the formation of an ordered polymer layer around the nanotubes. Fitting their experimental results with micromechanical models, the authors deduced that the stress transfer between nanotubes and polymer matrix was poor. Hegde et al. [18], comparing results from different amorphous polymer matrix reinforced with CNTs, found that the elastic properties of the composite increase only when nanotubes nucleate crystallization. Watts and Hsu [15] investigated the strength of the interface through examination of the surface fracture in an MPC-DEA polymer matrix reinforced with CNTs. TEM images at the crack surface showed that the surface of the pulled-out nanotubes was clean (i.e. no polymer particles were attached to them) denoting poor adhesion between CNTs and matrix. Similar results were also reported for CNTs embedded in polystyrene [17] and epoxy [13,14] matrices. Using Raman spectroscopy, Wang et al. [16] suggested that the variation in the Young's modulus of CNT-epoxy composites induced by different degrees and types of functionalization groups on the nanotubes surface was caused by changes of the interfacial molecular structure.

However, it is worth mentioning that other authors reported strong atomic interactions between polymer matrix and nonfunctionalized nanotubes. Qian and coworkers [53,54] observed fractured nanotubes at the crack surface in CNT-polystyrene composites suggesting a good load transfer between CNTs and polymer matrix. By using pull-out tests, good adhesion was also reported in CNT-epoxy composites [55] and CNT-polyethylene butane composites [2]. However, in these cases the pull-out force was not always parallel to the nanotube axis. Thus, the possible sliding of the embedded part of the nanotube along the interface surface during pull-out might have induced an overestimation of the interfacial properties [15]. Moreover, the elastic mechanical properties of the interface were not compared to those of the interphase.

Therefore, we limit the present study to nonfunctionalized CNT-polymer composites where the CNT-matrix adhesion is poor and CNTs nucleate a highly ordered region of polymer matrix. At the same time, this study allows for the assessment of the effect of the interphase on the composite elastic properties.

### 2.5. Size effect

As shown in Fig. 6, the component $C_{xx}$ of the elasticity tensor, characterizing the stiffness of the composite in the axial direction, decreases by increasing the nanotube diameter. A similar trend was observed with atomistic simulations of CNTs embedded in polypropylene [22], polyvinyl chloride [37] and EPON 862® epoxy resin 7. Here, the size effect is solely determined by the interphase as the only component of the CNT-polymer composites having a reinforcement effect. In particular, the variation of $C^c_{xx}$ and $C^c_{xy}$ with respect to the CNT diameter $d$ can be motivated by the trend of the interphase volume fraction $v^{ip}$ with respect to $d$ (this will be discussed in further details in Section 3). As shown in Figs. 3–4, by increasing the diameter $d$, despite the increased ordering of the interphase atomic structure, the volume fraction of the interphase (i.e. the reinforcement phase) decreases and, consequently, also the stiffness of the composite in the $x$-direction: the lower the interphase volume fraction, the softer the reinforcement.

## 3. Interphase as an equivalent continuum 3-D fiber

In this section we define a continuum model that is mechanically equivalent to the discrete atomistic model shown earlier. This allows the estimation of the elastic properties (i.e, Young's modulus and Poisson's ratio) of the interphase, here modeled through an equivalent 3-D fiber, that are required for the micromechanical modeling of the nonfunctionalized CNT-polymer composites in Section 4. Moreover, CNT diameter-induced size effects on the elastic properties of the interphase are discussed in Section 3.2.

The previous MM simulations showed that only the interphase provides reinforcement. Due to weak non-bonded interactions between polymer matrix and CNT atoms, the contribution of the

CNT is negligible. Therefore, as shown in Fig. 1b, the proposed intermediate continuum micromechanical model consists only of the bulk polymer, assumed as homogeneous, and an equivalent continuum 3-D fiber (representing the interphase region) with homogeneous properties while interface and CNT are not taken into account. Accordingly, only the Young's modulus and Poisson's ratio of the bulk polymer matrix and the three-dimensional fiber, employed to represent the interphase, are estimated in this section.

The Young's modulus $E^{\mathrm{m}}$ and the Poisson's ratio $\nu^{\mathrm{m}}$ of the bulk polymer matrix are derived from the estimated $C^{\mathrm{m}}_{xx}$ and $C^{\mathrm{m}}_{xy}$. Since the matrix is isotropic, following [56],

$$E^{\mathrm{m}} = \frac{C^{\mathrm{m}}_{xx}C^{\mathrm{m}}_{xx} + C^{\mathrm{m}}_{xx}C^{\mathrm{m}}_{xy} - 2C^{\mathrm{m}}_{xy}C^{\mathrm{m}}_{xy}}{C^{\mathrm{m}}_{xx} + C^{\mathrm{m}}_{xy}} \quad \text{and} \qquad \nu^{\mathrm{m}} = \frac{C^{\mathrm{m}}_{xy}}{C^{\mathrm{m}}_{xy} + C^{\mathrm{m}}_{xx}}. \tag{15}$$

Accordingly, $E^{\mathrm{m}}$ and $\nu^{\mathrm{m}}$ resulted equal to 3.04 GPa and 0.36, respectively, values in the typical range for glassy polymers [57].

As illustrated in Fig. 1b, the interphase is modeled by an equivalent continuum solid fiber shaped as a hollow cylinder. Its dimensions coincide with those of the interphase region: the length is equal to that of the embedded nanotube ($l$) while inner radius $r^{\mathrm{i}} = d/2 + t^{\mathrm{if}}$ and outer radius $r^{\mathrm{f}} = d/2 + t^{\mathrm{if}} + t^{\mathrm{ip}}$. Since in Section 4 we model the reinforcement provided by the interphase through one-dimensional elements, the equivalent continuum fibers are assumed isotropic and the mechanical properties are averaged through the thickness.

Young's modulus $E^{\mathrm{f}}$ and Poisson's ratio $\nu^{\mathrm{f}}$ of the equivalent continuum solid fiber are determined through an identification procedure where the axial stiffness of the atomistic model and that of the intermediate continuum micromechanical model are compared. This problem is formulated as

$$\text{find} \quad \min_{p} f(p), \tag{16}$$

with $p = [E^{\mathrm{f}}, \nu^{\mathrm{f}}]$ the vector of unknown parameters and $f(p)$ the cost function

$$f(p) = \frac{1}{2}\sum_{i=x,y}\left(\frac{C^{\mathrm{c}}_{xi} - \tilde{C}^{\mathrm{c}}_{xi}\left(E^{\mathrm{f}}, \nu^{\mathrm{f}}\right)}{C^{\mathrm{c}}_{xi}}\right)^2, \tag{17}$$

where $C^{\mathrm{c}}_{xi}$ are the elastic components of the CNT-polymer composites derived from the MM simulations (Section 2.3) and $\tilde{C}^{\mathrm{c}}_{xi}$ those from the corresponding continuum models in Fig. 1b. The least-square problem (16) was solved using the Gauss-Newton algorithm [58]. This iterative procedure was terminated when both $f(p)$ and the infinity norm of the gradient $\nabla_p f(p)$ were lower than $10^{-10}$.

### 3.1. Numerical solution

The elastic components $\tilde{C}^{\mathrm{c}}_{xx}$ and $\tilde{C}^{\mathrm{c}}_{xy}$ of the continuum model in Fig. 1b have been derived with isogeometric analysis. Due to the hollow cylindrical shape of the equivalent continuum three-dimensional fiber, isogeometric finite elements [59] were employed. Cubic Non-Uniform B-spline (NURBS) basis functions were used to exactly represent the equivalent continuum fiber and bulk matrix geometries, and at the same time to approximate the corresponding displacement fields. As for the MM tensile tests, periodic boundary conditions in all directions together with the macrostrain tensor (11) have been enforced. Due to symmetry with respect to planes $xy$, $xz$ and $yz$, only an eight of the full model (see Fig. 7a) is considered and the corresponding boundary conditions are depicted in Fig. 7b (see Appendix A for details).

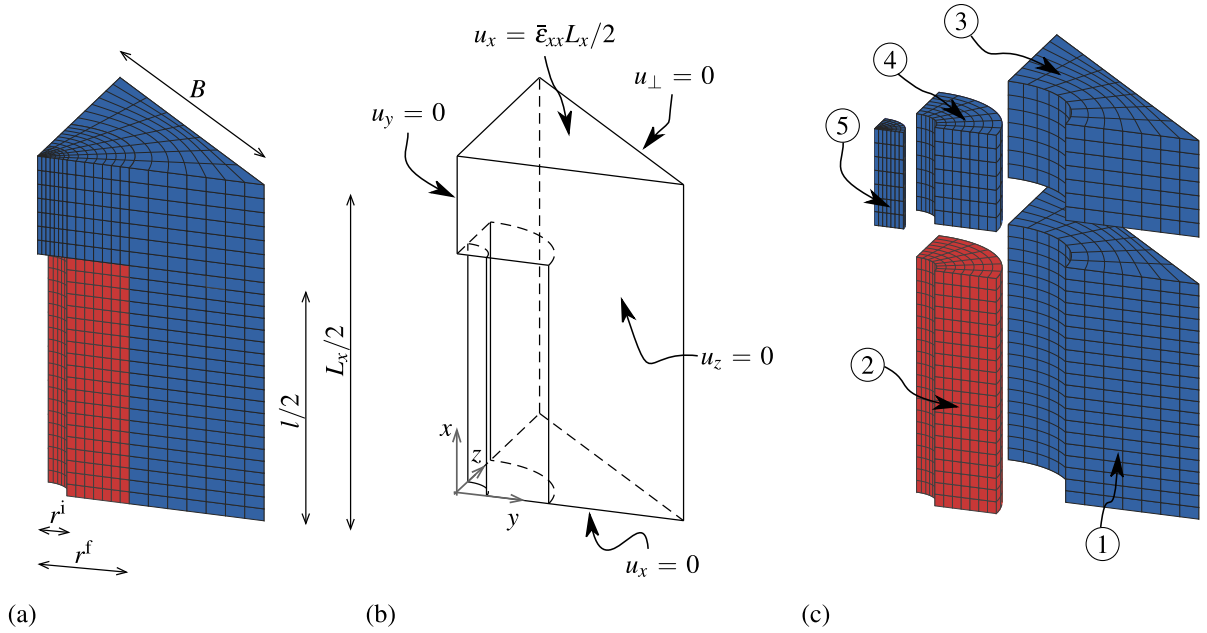


**Fig. 7.** (a) NURBS isogeometric model of the equivalent continuum (only an eight of the composite is considered due to symmetry). The bulk matrix is in blue, the equivalent continuum fiber in red. Quantities $r^{\mathrm{i}}$ and $r^{\mathrm{f}}$ refer to the inner and outer radius of the equivalent continuum fiber, respectively, $l$ its length and $L_x$ and $B$ denote the RVE size. (b) Schematic of the applied boundary conditions ($u_\perp$ denotes displacements orthogonal to the considered face of the model). (c) Exploded view of the isogeometric model showing the five NURBS patches and numbering of the different NURBS patches. (For interpretation of the references to colour in this figure legend, the reader is referred to the web version of this article.)

A NURBS multi-patch code [59,60] was employed to generate the isogeometric model. As illustrated in Fig. 7c, the model is defined by five patches: one for the equivalent continuum fiber and four for the bulk polymer matrix. According to Hughes et al. [59], the geometry of each patch is defined by

$$S(\xi,\eta,\zeta) = \sum_{i=1}^{n_\xi}\sum_{j=1}^{n_\eta}\sum_{i=k}^{n_\zeta} N_{i,p}(\xi)M_{j,q}(\eta)L_{k,r}(\zeta)B_{i,j,k}, \tag{18}$$

where $\xi$, $\eta$ and $\zeta$ are coordinates in the so-called parameter space, $N_{i,p}(\xi)$, $M_{j,q}(\eta)$ and $L_{k,r}(\zeta)$ NURBS basis functions of degree $p$, $q$ and $r$, respectively, and $B_{i,j,k}$ the control points (the reader is referred to Hughes et al. [59] for more details on NURBS geometries and isogeometric analysis). NURBS basis functions $N_{i,p}(\xi)$, $M_{j,q}(\eta)$ and $L_{k,r}(\zeta)$ are defined by the knot vectors $\Xi = [\xi_1, \xi_2, \ldots, \xi_{n_\xi+p+1}]$, $\mathscr{H} = [\eta_1, \eta_2, \ldots, \eta_{n_\eta+q+1}]$ and $\mathscr{Z} = [\zeta_1, \zeta_2, \ldots, \zeta_{n_\zeta+r+1}]$, respectively. Parameters $n_\xi$, $n_\eta$ and $n_\zeta$ indicate the number of basis functions $N_{i,p}(\xi)$, $M_{j,q}(\eta)$ and $L_{k,r}(\zeta)$. Moreover, each control point $B_{i,j,k}$ is associated to a weight $w_{i,j,k}$. Therefore, each NURBS patch is defined by a set of knot vectors, control points and weight. The full data structure is provided in Appendix B.

The $k$-refinement approach [59] has been employed to increase the degree of the NURBS basis functions to cubic and insert new knots along the $\xi$, $\eta$ and $\zeta$ directions until convergence in the values of $E^f$ and $\nu^f$ (see Fig. 8). In particular, knots were inserted such that the knot vectors were uniform (i.e. evenly spaced knots) and the dimensions of the elements in the three directions close to each others. The final number of knots along $\xi$, $\eta$ and $\zeta$ is reported in Table 3 (the same discretization has been used for all the CNT-polymer composites).

### 3.2. Size effects

Fig. 9 shows the Young's modulus $E^f$ and the Poisson's ratio $\nu^f$ of the equivalent continuum fiber obtained from the parameter estimation procedure described in the previous section. The CNT diameter influences both $E^f$ and $\nu^f$. The Young's modulus increases with the diameter $d$ of the embedded nanotube while the Poisson's ratio decreases. Therefore, the overall stiffness of the interphase increases with $d$. This was expected as higher ordering in the interphase was observed when increasing the nanotube diameter [19,20].

**Table 3**
Number of knots along $\xi$, $\eta$ and $\zeta$ (denoted by $m_\xi$, $m_\eta$ and $m_\zeta$, respectively) for the five NURBS patches used in the estimation of the Young's modulus $E^f$ and Poisson's ratio $\nu^f$ of the equivalent continuum fiber.

| Patch | $m_\xi$ | $m_\eta$ | $m_\zeta$ |
|---|---|---|---|
| 1 | 21 | 8 | 8 |
| 2 | 21 | 8 | 8 |
| 3 | 8 | 8 | 8 |
| 4 | 8 | 8 | 8 |
| 5 | 8 | 8 | 8 |

Although the stiffness of the equivalent continuum fiber increases with the CNT diameter, the opposite trend was observed in Section 2.3 for the components of the elasticity tensor of the composite: the bigger the $d$, the softer the CNT-polymer composite. Nevertheless, this is a consequence of the decreasing volume fraction of interphase $v^{ip}$ in the composites reinforced with nanotubes of bigger diameters (see Fig. 4). Therefore, the results in Figs. 4 and 9 indicate that $v^{ip}$ plays a central role in the value of the mechanical properties of the CNT-polymer composites.

## 4. Micromechanical models for CNT-polymer composites

Having defined the elastic properties of bulk polymer and equivalent continuum fiber, we can investigate the macroscopic mechanical response of CNT-polymer composites. Due to the negligible effect of the CNT on the mechanical response of the composite, the micromechanical model for the CNT-polymer composite considers only the polymer matrix and the interphase as in the continuum model studied in the previous section. Moreover, with reference to real composites, the equivalent continuum fiber can be modeled as a one-dimensional fiber due to the high aspect ratio of the real nanotubes —throughout the rest of the paper the term “fiber” is used to refer to the one-dimensional equivalent continuum fiber. To model CNT-polymer composites with realistic nanotube volume fractions, thus with a high number of fibers as shown in Fig. 1c, the Embedded Reinforcement Method (ERM) is adopted. This numerical procedure is employed in the analysis of periodic RVEs with different CNT volume fractions and to investigate CNT diameter-induced effects. The numerical results are then compared to estimate from various analytical micromechanical models in Section 5.

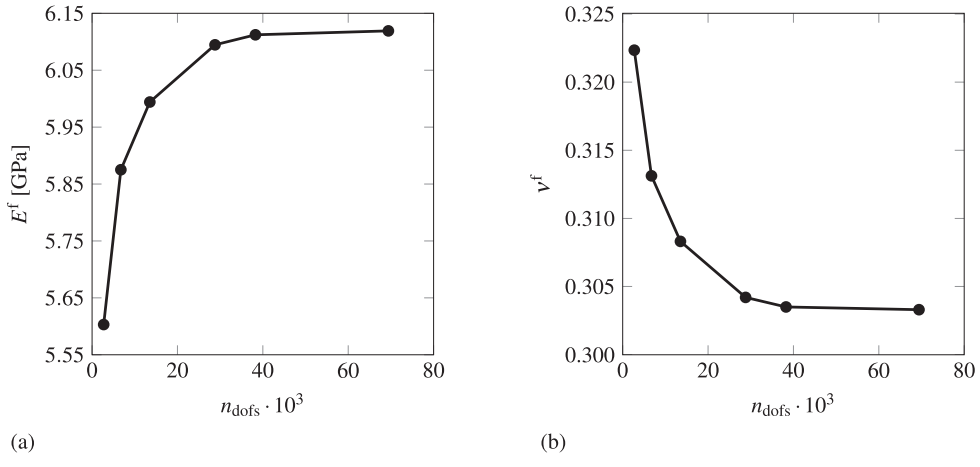


**Fig. 8.** Convergence of the estimated (a) $E^f$ and (b) $\nu^f$ with respect to the number of degrees of freedom $n_{dofs}$ for an (8,8)-polymer composite.

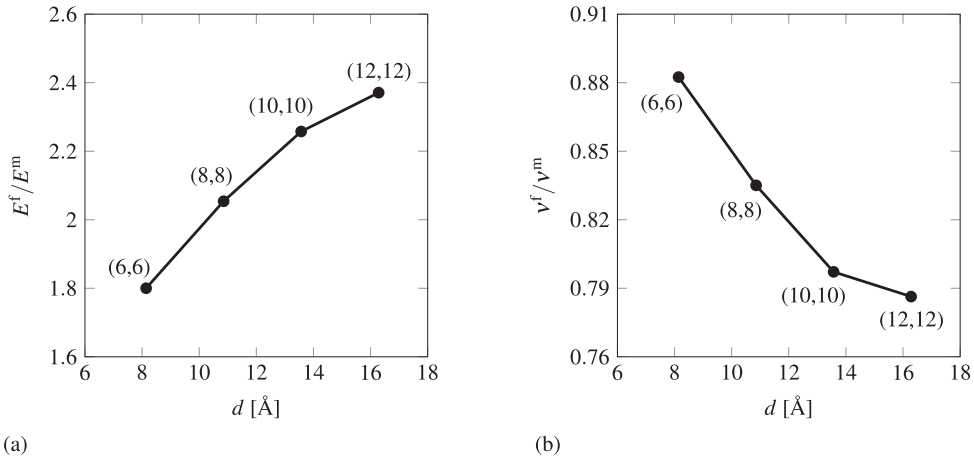


**Fig. 9.** (a) Young's modulus $E^f$ and (b) Poisson's ratio $\nu^f$ of the equivalent continuum fiber in $(n,n)$-polymer composites as a function of the nanotube $d$. Results have been normalized with respect to the polymer Young's modulus $E^m = 3.04$ GPa and Poisson's ratio $\nu^m = 0.36$. Since the ordering of the interphase atomic structure increases with the CNT diameter [20], $E^f$ increases with $d$ while the opposite trend is observed for $\nu^f$.

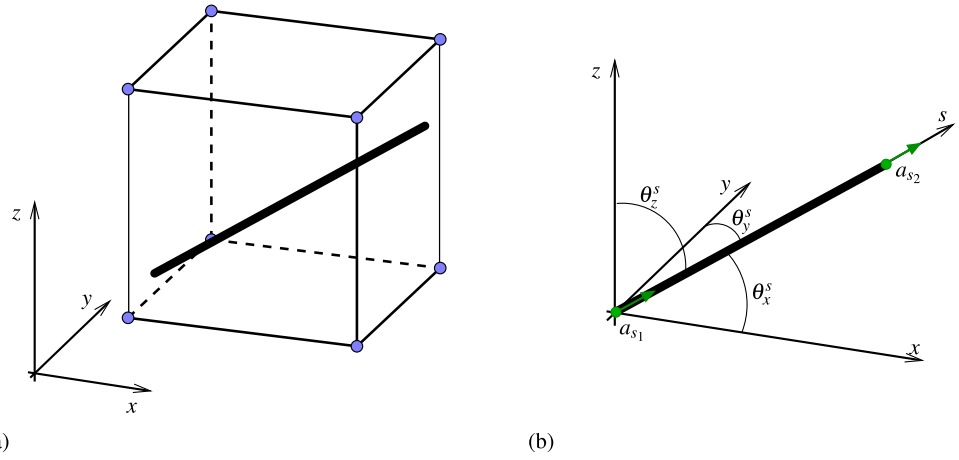


**Fig. 10.** (a) A hexahedral finite element with one embedded fiber: degrees of freedom (blue circles) are located only at the nodes of the embedding element. (b) Global coordinate system $(x, y, z)$ and fiber local axis $s$ (local displacements $a_{s_1}$ and $a_{s_2}$ at the fiber endpoints in green). (For interpretation of the references to colour in this figure legend, the reader is referred to the web version of this article.)

### 4.1. The embedded reinforcement method

The embedded reinforcement method [25,61] allows to efficiently incorporate fibers into a discretized continuum without actually meshing them as shown in Fig. 10a where a discrete fiber is embedded into a 3-D element. Although this model can be modified to incorporate fiber slip [62,63], here fibers are perfectly bonded to the matrix since there is no relative displacement between interphase and surrounding polymer.

For completeness, the derivation of the discrete set of equations governing the mechanical response of an element with one embedded fiber is reported next. We consider an elastic body with total volume $\Omega$ subdivided into matrix ($\Omega^m$) and fiber ($\Omega^f$) parts. In the absence of the external load, the principle of virtual work can be written as

$$\int_{\Omega^m} \nabla^s \delta \boldsymbol{u}^m : \boldsymbol{C}^m : \nabla^s \boldsymbol{u}^m \, d\Omega^m + \int_{\Omega^f} \left( \delta u^f_{,s} \left( E^f - E^m \right) u^f_{,s} \right) d\Omega^f = 0, \tag{19}$$

where $\boldsymbol{C}^m$ is the elasticity tensor of the bulk polymer (see (14)), $E^f$ and $E^m$ are the equivalent continuum fiber and bulk polymer elastic moduli derived in Section 3, $\nabla^s$ is the symmetric-gradient operator, $\delta$ denotes variation, and we used subscript notation for differentiation (a derivative with respect to the fiber local axis is indicated by the subscript "$,s$"). We exclude bulk material in the fiber domain by using the effective elastic moduli $(E^f - E^m)$ in the second term of (19). The displacement components $\boldsymbol{u}^m$ of a bulk element with $n$ nodes (for trilinear hexahedral elements, $n$ is equal to 8) can be discretized at any arbitrary point $\boldsymbol{x}$ through

$$\boldsymbol{u}^m(\boldsymbol{x}) = \sum_{i=1}^{n} N_i^m(\boldsymbol{x}) \boldsymbol{u}_i(\boldsymbol{x}) \tag{20}$$

with $N_i^m$ the shape functions of the bulk element and $\boldsymbol{u}_i$ the corresponding degrees of freedom. Thus, the discretized displacements and strains can be written in matrix form as

$$\boldsymbol{u}^m(\boldsymbol{x}) = \boldsymbol{N}^m \boldsymbol{u} \quad \text{and} \tag{21a}$$

$$\boldsymbol{\varepsilon}^{\mathrm{m}}(\boldsymbol{x}) = \boldsymbol{B}^{\mathrm{m}}\boldsymbol{u}, \tag{21b}$$

respectively, where $\boldsymbol{N}^{\mathrm{m}}$ and $\boldsymbol{B}^{\mathrm{m}}$ are matrices containing shape functions and corresponding derivatives, and $\boldsymbol{u}$ is the element displacement vector. The scalar fiber displacement $u^{\mathrm{f}}$ along the fiber local axis $s$ is approximated using one-dimensional linear Lagrangian shape functions as

$$u^{\mathrm{f}}(s) = N^{\mathrm{f}}_{s_1}(s)a_{s_1} + N^{\mathrm{f}}_{s_2}(s)a_{s_2}, \tag{22}$$

where $N^{\mathrm{f}}_{s_1}$ and $N^{\mathrm{f}}_{s_2}$ are the shape functions attributed to the fiber end points $s_1$ and $s_2$, respectively, while $a_{s_1}$ and $a_{s_2}$ are the corresponding local displacements (see Fig. 10b). The fiber displacement is transferred from the local fiber coordinate system ($s$) to the global coordinate system ($x$, $y$, $z$) by means of

$$\begin{aligned} u^{\mathrm{f}}(s) = \Big[ & N^{\mathrm{f}}_{s_1}\cos(\theta^s_x)\, N^{\mathrm{f}}_{s_1}\cos\left(\theta^s_y\right) N^{\mathrm{f}}_{s_1}\cos(\theta^s_z) \\ & N^{\mathrm{f}}_{s_2}\cos(\theta^s_x)\, N^{\mathrm{f}}_{s_2}\cos\left(\theta^s_y\right) N^{\mathrm{f}}_{s_2}\cos(\theta^s_z)\Big] \begin{bmatrix} \boldsymbol{u}^{\mathrm{f}}_{s_1} \\ \boldsymbol{u}^{\mathrm{f}}_{s_2} \end{bmatrix} \end{aligned} \tag{23}$$

with $\boldsymbol{u}^{\mathrm{f}}_{s_i} = [a^{\mathrm{f}}_{x_i}, a^{\mathrm{f}}_{y_i}, a^{\mathrm{f}}_{z_i}]^{\mathrm{T}}$ the global displacement vector at fiber endpoints and $\theta^s_i$ (with $i = x, y, z$) the fiber orientation angles. The derivatives of (23) with respect to the fiber axis are expressed as

$$u^{\mathrm{f}}_{,s}(\boldsymbol{x}) = \boldsymbol{B}^{\mathrm{f}}\boldsymbol{H}\boldsymbol{u}, \tag{24}$$

with

$$\begin{aligned} \boldsymbol{B}^{\mathrm{f}} = \Big[ & N^{\mathrm{f}}_{s_1,s}\cos(\theta^s_x)\ N^{\mathrm{f}}_{s_1,s}\cos\left(\theta^s_y\right)\ N^{\mathrm{f}}_{s_1,s}\cos(\theta^s_z) \\ & N^{\mathrm{f}}_{s_2,s}\cos(\theta^s_x)\ N^{\mathrm{f}}_{s_2,s}\cos\left(\theta^s_y\right)\ N^{\mathrm{f}}_{s_2,s}\cos(\theta^s_z)\Big] \end{aligned} \tag{25}$$

and

$$\boldsymbol{H} = \begin{bmatrix} N^{\mathrm{m}}_1(\boldsymbol{s}_1) & 0 & 0 & \cdots & N^{\mathrm{m}}_n(\boldsymbol{s}_1) & 0 & 0 \\ 0 & N^{\mathrm{m}}_1(\boldsymbol{s}_1) & 0 & \cdots & 0 & N^{\mathrm{m}}_n(\boldsymbol{s}_1) & 0 \\ 0 & 0 & N^{\mathrm{m}}_1(\boldsymbol{s}_1) & \cdots & 0 & 0 & N^{\mathrm{m}}_n(\boldsymbol{s}_1) \\ N^{\mathrm{m}}_1(\boldsymbol{s}_2) & 0 & 0 & \cdots & N^{\mathrm{m}}_n(\boldsymbol{s}_2) & 0 & 0 \\ 0 & N^{\mathrm{m}}_1(\boldsymbol{s}_2) & 0 & \cdots & 0 & N^{\mathrm{m}}_n(\boldsymbol{s}_2) & 0 \\ 0 & 0 & N^{\mathrm{m}}_1(\boldsymbol{s}_2) & \cdots & 0 & 0 & N^{\mathrm{m}}_n(\boldsymbol{s}_2) \end{bmatrix}, \tag{26}$$

where $\boldsymbol{H}$ is the transformation matrix mapping fiber displacements $\boldsymbol{u}^{\mathrm{f}}_{s_i}$ into bulk element displacements $\boldsymbol{u}$, while $\boldsymbol{s}_1$ and $\boldsymbol{s}_2$ are the coordinates of the fiber endpoints in the bulk element coordinate system. Finally, introducing the discretized interpolations of matrix (21b) and fiber (24) derivatives into the weak form of the momentum equation (19) yields the stiffness matrix

$$\boldsymbol{K} = \int_{\Omega^{\mathrm{m}}} \boldsymbol{B}^{\mathrm{mT}}\boldsymbol{C}^{\mathrm{m}}\boldsymbol{B}^{\mathrm{m}}\,\mathrm{d}\Omega + A^{\mathrm{f}}\int_{l^{\mathrm{f}}} \boldsymbol{H}^{\mathrm{T}}\boldsymbol{B}^{\mathrm{f}^{\mathrm{T}}}\left(E^{\mathrm{f}} - E^{\mathrm{m}}\right)\boldsymbol{B}^{\mathrm{f}}\boldsymbol{H}\,\mathrm{d}s \tag{27}$$

of an element with an embedded fiber where, since a uniform cross sectional area $A_{\mathrm{f}}$ is assumed for the fiber, the fiber volume integral in (19) is replaced by an equivalent line integral over the portion of fiber $l^{\mathrm{f}}$ embedded in the solid element. In the case of multiple fibers embedded in a single element, the total stiffness matrix

$$\begin{aligned} \boldsymbol{K} = & \int_{\Omega^{\mathrm{m}}} \boldsymbol{B}^{\mathrm{mT}}\boldsymbol{C}^{\mathrm{m}}\boldsymbol{B}^{\mathrm{m}}\,\mathrm{d}\Omega \\ & + \sum_{i=1}^{n_{\mathrm{f}}} A^{\mathrm{f}}_i \int_{l^{\mathrm{f}}_i} \boldsymbol{H}^{\mathrm{T}}_i\boldsymbol{B}^{\mathrm{fT}}_i\left(E^{\mathrm{f}}_i - E^{\mathrm{m}}\right)\boldsymbol{B}^{\mathrm{f}}_i\boldsymbol{H}_i\,\mathrm{d}s_i, \end{aligned} \tag{28}$$

in which $n_{\mathrm{f}}$ is the number of fibers in the solid element. As shown in (27) and (28), the total stiffness matrix of a solid element for the composite material is given by the sum of the stiffness matrix of the bulk polymer matrix and the stiffness contribution(s) of the embedded one-dimensional fiber(s).

#### 4.1.1. Effective mechanical properties and periodic boundary conditions

The macroscopic elastic properties of the CNT-polymer composite are derived through computational homogenization. For a generic RVE, Hooke's law is expressed as

$$\begin{bmatrix} \overline{\sigma}_{xx} \\ \overline{\sigma}_{yy} \\ \overline{\sigma}_{zz} \\ \overline{\sigma}_{xy} \\ \overline{\sigma}_{xz} \\ \overline{\sigma}_{yz} \end{bmatrix} = \begin{bmatrix} C^{\mathrm{c}}_{11} & C^{\mathrm{c}}_{12} & C^{\mathrm{c}}_{13} & C^{\mathrm{c}}_{14} & C^{\mathrm{c}}_{15} & C^{\mathrm{c}}_{16} \\ C^{\mathrm{c}}_{21} & C^{\mathrm{c}}_{22} & C^{\mathrm{c}}_{23} & C^{\mathrm{c}}_{24} & C^{\mathrm{c}}_{25} & C^{\mathrm{c}}_{26} \\ C^{\mathrm{c}}_{31} & C^{\mathrm{c}}_{32} & C^{\mathrm{c}}_{33} & C^{\mathrm{c}}_{34} & C^{\mathrm{c}}_{35} & C^{\mathrm{c}}_{36} \\ C^{\mathrm{c}}_{41} & C^{\mathrm{c}}_{42} & C^{\mathrm{c}}_{43} & C^{\mathrm{c}}_{44} & C^{\mathrm{c}}_{45} & C^{\mathrm{c}}_{46} \\ C^{\mathrm{c}}_{51} & C^{\mathrm{c}}_{52} & C^{\mathrm{c}}_{53} & C^{\mathrm{c}}_{54} & C^{\mathrm{c}}_{55} & C^{\mathrm{c}}_{56} \\ C^{\mathrm{c}}_{61} & C^{\mathrm{c}}_{62} & C^{\mathrm{c}}_{63} & C^{\mathrm{c}}_{64} & C^{\mathrm{c}}_{65} & C^{\mathrm{c}}_{66} \end{bmatrix} \begin{bmatrix} \overline{\varepsilon}_{xx} \\ \overline{\varepsilon}_{yy} \\ \overline{\varepsilon}_{zz} \\ \overline{\varepsilon}_{xy} \\ \overline{\varepsilon}_{xz} \\ \overline{\varepsilon}_{yz} \end{bmatrix}, \tag{29}$$

where the parameters $C^{\mathrm{c}}_{ij}$ are the components of the homogenized effective elasticity tensor for the composite material. These are determined imposing the six sets of boundary conditions in Table 4 (the full set of constraint equations to be imposed on RVE faces, edges and vertices are listed in Appendix A). Then, for each boundary condition, the corresponding local stress field $\boldsymbol{\sigma}$ in the composite is determined using the ERM described in Section 4.1. Consequently, the macrostrain tensor $\overline{\boldsymbol{\sigma}}$ is calculated as

$$\overline{\boldsymbol{\sigma}} = \frac{1}{V}\int_V \boldsymbol{\sigma}\mathrm{d}V, \tag{30}$$

where $V$ is the volume of the RVE. Hence, knowing the macrostrain and macrostress tensors $\overline{\boldsymbol{\varepsilon}}$ and $\overline{\boldsymbol{\sigma}}$, respectively, the effective elasticity tensor components $C^{\mathrm{c}}_{ij}$ are derived from (29).

Once the effective mechanical properties in (29) are known, we can provide an estimate of the engineering constants (Young's modulus, shear modulus and Poisson's ratio). For composites with perfectly aligned CNTs along the $x$ axis, the RVE is transversely isotropic and the elastic constitutive matrix is

$$\boldsymbol{C}^{\mathrm{c}} = \begin{bmatrix} C^{\mathrm{c}}_{xx} & C^{\mathrm{c}}_{xy} & C^{\mathrm{c}}_{xy} & 0 & 0 & 0 \\ C^{\mathrm{c}}_{xy} & C^{\mathrm{c}}_{yy} & C^{\mathrm{c}}_{yz} & 0 & 0 & 0 \\ C^{\mathrm{c}}_{xy} & C^{\mathrm{c}}_{yz} & C^{\mathrm{c}}_{yy} & 0 & 0 & 0 \\ 0 & 0 & 0 & 2G^{\mathrm{c}}_{xy} & 0 & 0 \\ 0 & 0 & 0 & 0 & 2G^{\mathrm{c}}_{yz} & 0 \\ 0 & 0 & 0 & 0 & 0 & 2G^{\mathrm{c}}_{yz} \end{bmatrix}. \tag{31}$$

Two of the five independent constants, the shear moduli $G^{\mathrm{c}}_{xy}$ and $G^{\mathrm{c}}_{yz}$, are known from (31) and, following 64, the remaining three are expressed according to

$$E^{\mathrm{c}}_{xx} = C^{\mathrm{c}}_{xx} - \frac{2C^{\mathrm{c}}_{xy}C^{\mathrm{c}}_{xy}}{C^{\mathrm{c}}_{yy} + C^{\mathrm{c}}_{yz}}, \tag{32a}$$

**Table 4**
Macrostrain tensor and derived components of $\boldsymbol{C}^{c}$ for uniaxial tension and transverse shear boundary condition.

| Boundary condition | Macrostrain tensor $\bar{\varepsilon}$ | Derived components of $\boldsymbol{C}^{c}$ |
|---|---|---|
| Uniaxial tension | $[0.1,\ 0,\ 0,\ 0,\ 0,\ 0]^{T}$ | $C^{c}_{i1}$ |
| | $[0,\ 0.1,\ 0,\ 0,\ 0,\ 0]^{T}$ | $C^{c}_{i2}$ |
| | $[0,\ 0,\ 0.1,\ 0,\ 0,\ 0]^{T}$ | $C^{c}_{i3}$ |
| Transverse shear | $[0,\ 0,\ 0,\ 0.1,\ 0,\ 0]^{T}$ | $C^{c}_{i4}$ |
| | $[0,\ 0,\ 0,\ 0,\ 0.1,\ 0]^{T}$ | $C^{c}_{i5}$ |
| | $[0,\ 0,\ 0,\ 0,\ 0,\ 0.1]^{T}$ | $C^{c}_{i6}$ |

$$E^{c}_{yy} = \frac{\left(C^{c}_{yy} - C^{c}_{yz}\right)\left(C^{c}_{yy}C^{c}_{xx} + C^{c}_{yz}C^{c}_{xx} - 2C^{c}_{xy}C^{c}_{xy}\right)}{C^{c}_{yy}C^{c}_{xx} - C^{c}_{xy}C^{c}_{xy}}, \quad \text{and} \tag{32b}$$

$$\nu^{c}_{xy} = \frac{C^{c}_{xy}}{C^{c}_{yy} + C^{c}_{yz}}. \tag{32c}$$

For randomly oriented fibers, the RVE is isotropic and the elastic constitutive matrix is expressed as

$$\boldsymbol{C}^{c} = \begin{bmatrix} \lambda^{c}+2\mu^{c} & \lambda^{c} & \lambda^{c} & 0 & 0 & 0 \\ \lambda^{c} & \lambda^{c}+2\mu^{c} & \lambda^{c} & 0 & 0 & 0 \\ \lambda^{c} & \lambda^{c} & \lambda^{c}+2\mu^{c} & 0 & 0 & 0 \\ 0 & 0 & 0 & \mu^{c} & 0 & 0 \\ 0 & 0 & 0 & 0 & \mu^{c} & 0 \\ 0 & 0 & 0 & 0 & 0 & \mu^{c} \end{bmatrix}, \tag{33}$$

where $\lambda^{c}$ and $\mu^{c}$ are the Lamé parameters. The corresponding Young's modulus and shear modulus are

$$E^{c} = \frac{\mu^{c}(3\lambda^{c} + 2\mu^{c})}{\lambda^{c} + \mu^{c}} \quad \text{and} \quad G^{c} = \mu^{c}, \tag{34}$$

respectively.

#### 4.1.2. RVE generation

The ERM has been used for the analysis of cubic periodic RVEs with equally long and randomly distributed fibers, here representing the interphases, either perfectly aligned along the $x$ direction or randomly oriented. The method used for the generation of the RVEs, implemented in Matlab®, followed the Random Sequential Adsorption algorithm [65–67]. Accordingly, fibers are added consecutively to the RVEs until a specific volume fraction is reached. In unidirectional fiber composites, all fibers are aligned along the $x$-axis while in randomly oriented fiber composites the orientation of each fiber is determined using the Matlab® function rand. For both unidirectional and randomly oriented fiber composites, the rand function is used to define the coordinates of one of the end points of a fiber. As the fiber length is a known parameter, the coordinates of the second end of a fiber can be easily derived. If this point lies outside the RVE, the exceeding part of the fiber is cut and shifted to the opposite boundary to enforce periodicity. To avoid fiber overlap, when a new fiber is added to the RVE we check that the distance between its axis and that of the exiting fibers is larger than twice the radius of the fibers (i.e., the outer radius of the interphase). If this condition is not satisfied, the fiber is removed and a new one is created. This process is repeated until the requirement for the minimum distance between fibers is fulfilled.

**Assessment of fibers orientation distribution**. Fiber orientation has a strong influence on the mechanical properties of the composite. Therefore, after the RVEs were created, the overall orientation of the fibers, also known as the orientation distribution, has been characterized. The orientation distribution was measured through the second order tensor of fiber orientation [68,69]. With reference to Fig. 11a, the orientation of a single fiber is defined by the unit vector $\boldsymbol{p}$ with components

$$p_1 = \sin\theta\cos\phi, \tag{35a}$$

$$p_2 = \sin\theta\sin\phi, \quad \text{and} \tag{35b}$$

$$p_3 = \cos\theta, \tag{35c}$$

where $\theta$ is the angle between the fiber axis and the $z$-axis, and $\phi$ is the angle between the projection of the fiber on the $xy$-plane and the $x$-axis. Accordingly, the second order tensor $\boldsymbol{a}$ of fiber order orientation is calculated as

$$\boldsymbol{a} = a_{ij} = \frac{1}{n^{CNT}}\sum_{k=1}^{n^{CNT}} p^{k}_{i}p^{k}_{j} = \begin{bmatrix} a_{11} & a_{12} & a_{13} \\ a_{12} & a_{22} & a_{23} \\ a_{13} & a_{23} & a_{33} \end{bmatrix} \tag{36}$$

with $n^{CNT}$ the number of fibers in the RVE. Only six of the nine components of $a_{ij}$ are independent due to its symmetry. Fig. 11b and c shows the second order tensor $\boldsymbol{a}$ for composites with fibers perfectly aligned along the $x$-axis and randomly oriented, respectively.

For an (8,8)-polymer composite with 6915 randomly oriented fibers, later used in our simulations,

$$a_{ij} = \begin{bmatrix} 0.330 & -0.003 & -0.003 \\ -0.003 & 0.339 & -0.003 \\ -0.003 & -0.003 & 0.331 \end{bmatrix}. \tag{37}$$

The second order tensor in (37) is very close to that in Fig. 11c, indicating that fibers can be considered as evenly oriented in the three directions. Analogous results were derived for all the RVEs used in our simulations. The second order tensor of fiber orientation was calculated also for RVEs with unidirectional fibers and it coincided with that in Fig. 11b.

#### 4.1.3. RVE dimensions

The size of the RVE should be sufficiently large to be statistically representative of the macroresponse of the composite and such that its mechanical properties do not depend on the dimensions of the inclusions [70–72]. In this case it seems reasonable to require that the RVE size should at least be larger than the nanotube length, typically in the range of some micrometers [14–55]. However, this would imply large RVEs with a very high number of CNTs due to their high aspect ratio and, consequently, a prohibitive computational effort.

To avoid this issue, before defining the size of the RVE, we determined the minimum length of the embedded fibers above which the elastic properties of the RVEs do not change. This allows for the generation of smaller RVEs with a lower number of fibers and, at the same time, avoids length effects in the mechanical properties of the composites (in this work we focus only on diameter-induced effects). Fig. 12 shows that $C^{c}_{xx}$ can be assumed constant for $l^{f} \geq 200$ nm as previously observed through multiscale simulations on CNT-polyimide composites [21].

Then, using $l^{f} = 200$ nm we investigated the effects induced by the RVEs size. This was performed through the analysis of $C^{c}_{xx}$

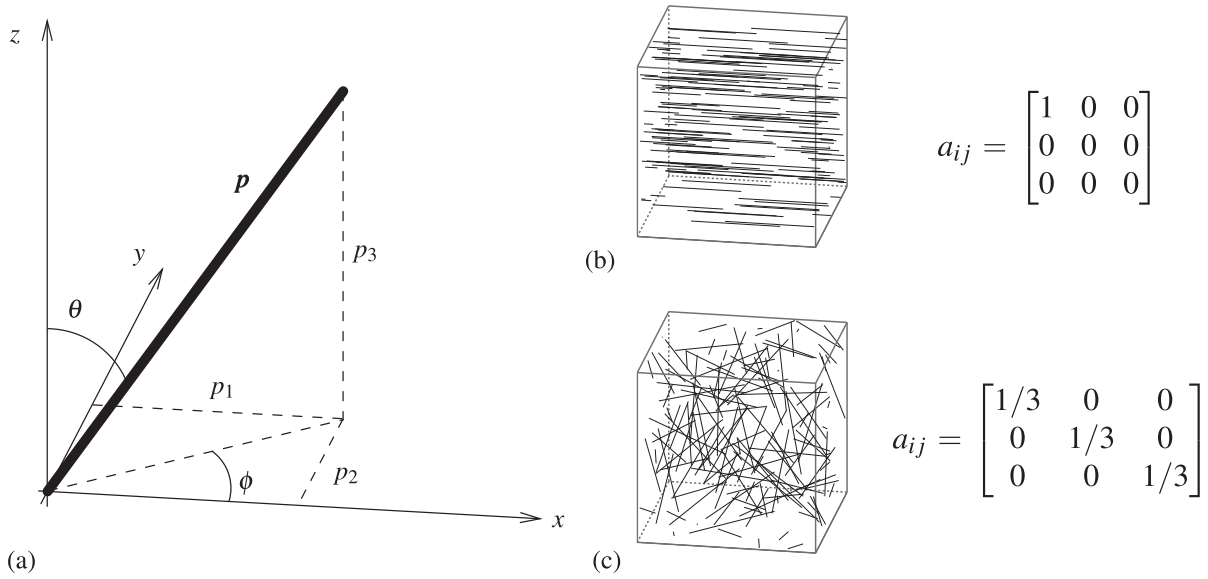


**Fig. 11.** (a) Definition of angles $\theta$ and $\phi$ used to calculate the orientation of a CNT (thick solid line) through the unit vector $\boldsymbol{p}$ with components $p_1$, $p_2$ and $p_3$. Composites with CNTs perfectly aligned along the $x$-axis (b) and randomly oriented CNTs (c).

changing the size $L$ of the cubic RVE. For each value of $L$, four different RVEs were created and the standard deviation from the mean value of $C^c_{xx}$ was calculated. This procedure was performed for CNT-polymer composites with $v^{CNT}$ equal to 0.6 and 1.5%. As shown in Fig. 13a and b, the dispersion is always lower than 2% and decreases when increasing $L$ similarly to the results in Reference [73]. For $L/l^f = 2$, standard deviation further decreases and the averaged values of $C^c_{xx}$ are more in line with those obtained for larger RVEs. Therefore, in our simulations the size of the RVE was assumed twice the length of the embedded fibers (i.e., 400 nm) as also suggested in other works on short fiber reinforced composites [66,74].

#### 4.1.4. Meshing the RVEs

As mentioned in Section 4.1 the RVEs are discretized using hexahedral finite elements. Since the fibers are uniformly distributed in the matrix and because of the modest stress concentration at the fiber ends, we employed uniform meshes for all the RVEs.

The size of the cubic hexahedral elements $L_e = L/n_{sub}$, where $n_{sub}$ is the number of subdivisions per RVE side, was determined from the variation of the RVE elastic properties while refining the mesh. This analysis was performed on the RVE with the highest number of embedded fibers, a (6,6)-polymer composite with $v^{CNT}$ equal to 2% (12293 CNTs). The length of the fibers and that of the RVE side were set equal to 200 and 400 nm according to the results in the previous section.

Fig. 14 shows that the difference between the estimated $E^c$ and $G^c$ with respect to the values obtained with the finer mesh (i.e., $n_{sub} = 30$) is negligible when $n_{sub} \geq 20$. Therefore, for all the simulations we adopted a uniform mesh with cubic hexahedral elements of size $L_e$ equal to $L/20$.

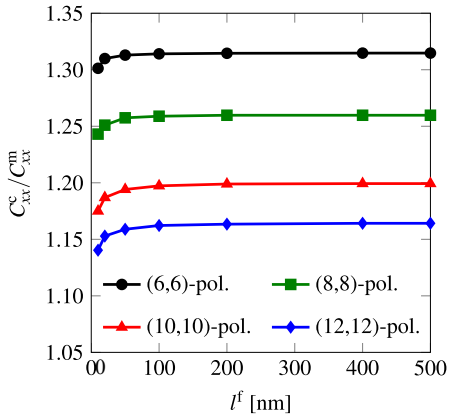


**Fig. 12.** Variation of $C^c_{xx}$ with the length $l^f$ of the embedded fibers. These results, normalized with respect to $C^m_{xx} = 5.14$ GPa, were derived with the ERM for different $(n,n)$-polymer composites with fibers aligned along the $x$ direction and $v^{CNT} = 1.5\%$. Similar results were observed for $C^c_{xy}$.

## 5. Elastic properties of the nanocomposite

In this section, we assess the influence of the reinforcement provided by the interphase on the macroscopic properties of the CNT-polymer composites. As shown in Table 5, we employed values of $v^{CNT}$ between 0.2 and 2.0% [17,18,53] to avoid intersections between different fibers (i.e., the interphase regions). Accordingly, the number of embedded fibers in the generated RVEs ranges from 307 to 12293 for both unidirectional and randomly oriented CNTs (see Fig. 15a and b, respectively). Three different RVEs were created for each configuration and results were averaged.

The elastic properties of the composites are derived through the modeling approach in Section 4 and some analytical micromechanical models discussed in the next section.

### 5.1. Analytical micromechanical models

Analytical micromechanical models are commonly used to estimate the mechanical properties of fiber reinforced materials. Some of the most frequently used micromechanical models are briefly summarized below. In the next sections, their predictions

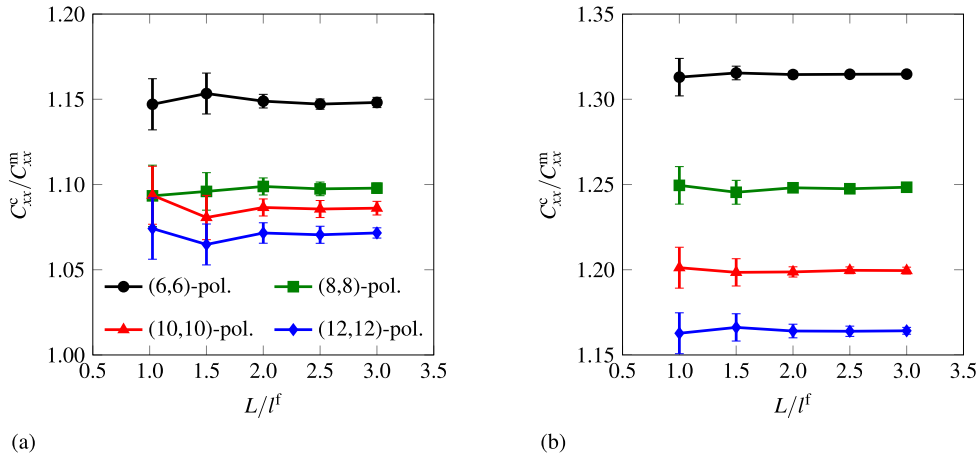


**Fig. 13.** Variation of $C^c_{xx}$ with the side $L$ of cubic RVEs for $(n,n)$-polymer composites with $v^{CNT}$ equal to (a) 0.6% and (b) 1.5%. The values of $C^c_{xx}$ and $L$ have been normalized with respect to $C^m_{xx} = 5.14$ GPa and the fiber length $l^f = 200$ nm, respectively. For each case, four different samples were considered. Error bars indicate standard deviations from the mean values of $C^c_{xx}$ denoted by the symbols.

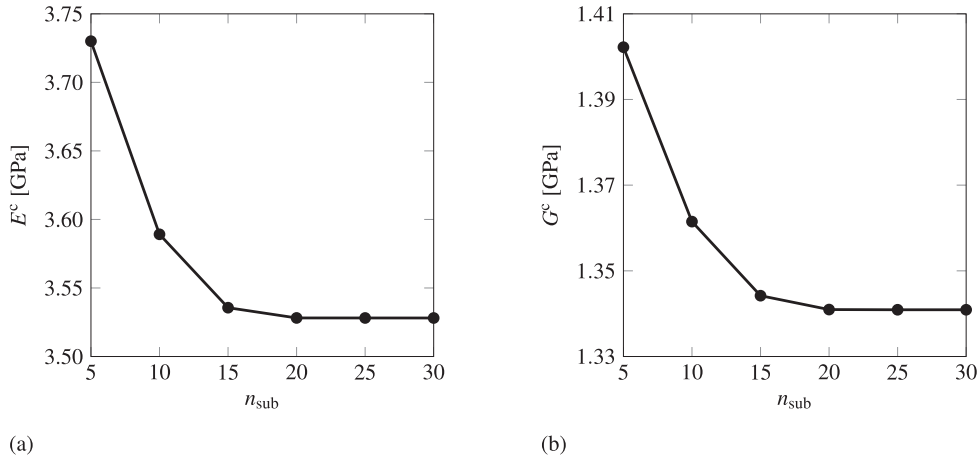


**Fig. 14.** Numerical convergence of $E^c$ and $G^c$ for a (6,6)-polymer composite with $v^{CNT} = 2\%$ (corresponding to 12293 CNTs).

**Table 5**
Number of embedded fibers in the RVEs.

| | $v^{CNT} = 0.2\%$ | $v^{CNT} = 0.6\%$ | $v^{CNT} = 1.0\%$ | $v^{CNT} = 1.5\%$ | $v^{CNT} = 2.0\%$ |
|---|---|---|---|---|---|
| (6,6)-polymer | 1229 | 3688 | 6146 | 9220 | 12293 |
| (8,8)-polymer | 691 | 2074 | 3457 | 5186 | 6915 |
| (10,10)-polymer | 443 | 1328 | 2213 | 3319 | 4425 |
| (12,12)-polymer | 307 | 922 | 1537 | 2305 | 3073 |

are compared with numerical results obtained with the embedded reinforcement method presented in Section 4.1.

Shear lag models [75] are typically employed to provide an analytical solution for the stress distribution in short fiber composites and an estimate of their mechanical properties. The classical formulation proposed by Cox [76] examines the axial stress along a single short fiber embedded in a continuous solid matrix. The matrix, assumed void free, is considered elastic and isotropic. The load is transferred from the matrix to the fiber through shear stresses at their interface where matrix and fibers are perfectly bonded. Based on the results from Ref. [76], for a composite reinforced with unidirectional perfectly aligned and equally spaced short fibers, with equal length and stiffness, the Young's modulus in the fibers direction (the $x$-axis in this work) is estimated through the modified rule of mixture

$$E^c_{xx} = \eta_l v^f E^f + \left(1 - v^f\right) E^m. \tag{38}$$

The variable $v^f$ is the fiber volume fraction (here coinciding with $v^{ip}$) and the coefficient $\eta_l$, which takes into account the aspect ratio

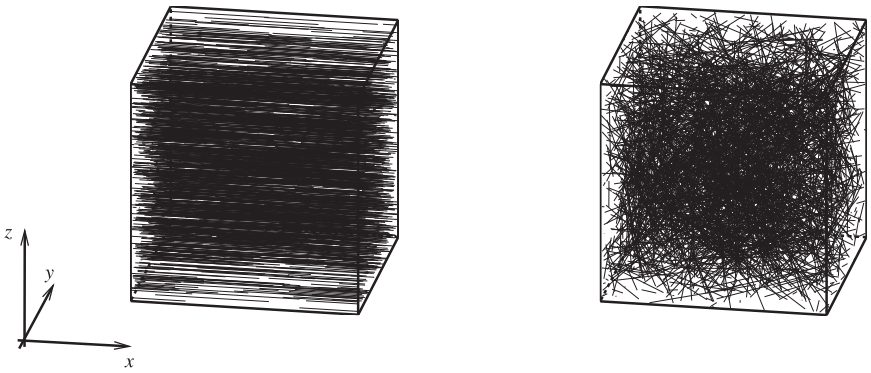


**Fig. 15.** Periodic RVEs of (8,8)-polymer composites with (a) unidirectional and (b) randomly oriented nanotubes with $\upsilon^{CNT} = 1\%$ (i.e., 3457 CNTs).

of the fibers [76], is calculated as

$$\eta_l = 1 - \frac{\tanh(\beta l/2)}{\beta l/2} \quad \text{with} \quad \beta = \sqrt{\frac{2G^m}{E^f (r^f)^2 \ln(R/r^f)}}, \tag{39}$$

where $G^m$ is the matrix shear modulus, $R$ is half the distance between the axis of the fibers [75], and $r^f$ is their radius. For randomly oriented fibers of equal length, Krenchel [77] proposed a modified version of (38):

$$E^c = \frac{1}{5}\eta_l \upsilon^f E^f + \left(1 - \upsilon^f\right) E^m. \tag{40}$$

The Halpin-Tsai model [64] is based on the same assumptions of the shear lag model and provides the following equation for the Young's modulus in the direction of the fibers:

$$E^c_{xx} = E^m \frac{1 + \xi_P \eta \upsilon^f}{1 - \eta \upsilon^f} \tag{41}$$

with

$$\eta = \frac{E^f/E^m - 1}{E^f/E^m + \xi} \quad \text{and} \quad \xi = 2l/d^f. \tag{42}$$

A modified version of (41), referred to as the Tsai-Pagano equation [78,79], has been proposed for the calculation of the Young's modulus of composites with randomly oriented fibers in 3-D:

$$E^c = E^m \left[\frac{3}{8}\frac{1 + \xi\eta\left(1 - \upsilon^f\right)}{1 - \eta\upsilon^f} + \frac{5}{8}\frac{1 + \xi\eta\left(1 - \upsilon^f\right)}{1 - \eta\upsilon^f}\right]. \tag{43}$$

Further, we have considered the micromechanical model proposed by Pan [80] for composite materials with randomly oriented fibers. Here, the Young's modulus is defined as

$$E^c = E^f \frac{\upsilon^f}{2\pi} + E^m\left(1 - \frac{\upsilon^f}{2\pi}\right). \tag{44}$$

Finally, the numerical results have been compared to the Hashin-Shtrikman bounds [81] derived through variational principles for statistically isotropic and nonhomogeneous composite materials. For the present composites, the lower and upper bounds (denoted with the superscripts $(-)$ and $(+)$) for the bulk and shear moduli are

$$K^{c(-)} = K^m + \frac{\upsilon^f}{\frac{1}{K^f - K^m} + \frac{3(1 - \upsilon^f)}{3K^m + 4G^m}}, \tag{45a}$$

$$K^{c(+)} = K^f + \frac{1 - \upsilon^f}{\frac{1}{K^m - K^f} + \frac{3\upsilon^f}{3K^f + 4G^f}}, \tag{45b}$$

$$G^{c(-)} = G^m + \frac{\upsilon^f}{\frac{1}{G^f - G^m} + \frac{6(1 - \upsilon^f)(K^m + 2G^m)}{5G^m(3K^m + 4G^m)}} \quad \text{and} \tag{45c}$$

$$G^{c(+)} = G^f + \frac{1 - \upsilon^f}{\frac{1}{G^m - G^f} + \frac{6\upsilon^f(K^f + 2G^f)}{5G^f(3K^f + 4G^f)}}, \tag{45d}$$

respectively. Consequently, the lower and upper bounds for the composite Young's modulus are

$$E^{c(-)} = \frac{9K^{(-)}G^{(-)}}{3K^{(-)} + G^{(-)}} \quad \text{and} \quad E^{c(+)} = \frac{9K^{(+)}G^{(+)}}{3K^{(+)} + G^{(+)}}. \tag{46}$$

### 5.2. Unidirectional reinforcement

Fig. 16a–e shows the Young's moduli $E^c_{xx}$, $E^c_{yy}$, the Poisson's ratio $\nu^c_{xy}$ and the shear moduli $G^c_{xy}$ and $G^c_{yz}$, respectively, as a function of the CNT volume fraction for composites with CNTs perfectly aligned along the $x$ direction. Results indicate an overall improvement of the stiffness with increasing CNT volume fraction. As depicted in Fig. 16a–b, the Young's moduli linearly increase with $\upsilon^{CNT}$ and, due to the unidirectional orientation of the embedded reinforcements, the major improvements are noticed in $E^c_{xx}$. Fig. 16c–e shows a neutral reinforcement effect on the Poisson's ratio and the shear moduli as their value coincides with those of the polymer matrix. This is due to the modeling of the interphases as one-dimensional fibers. In analogy with rigid line inclusion solutions under remote in-plane stresses [82,83], a one-dimensional "rigid" inclusion does not perturb the stress field of the embedding

matrix undergoing shear deformation parallel to its axis. Therefore, unidirectional one-dimensional reinforcements aligned along the $x$-direction do not change $G^c_{xy}$ (see Fig. 16d). Worth noting is that analogous results are found for $\nu^c_{xy}$ and $G^c_{yz}$ as shown in Fig. 16c and e, respectively.

In the macroscopic model, unidirectional fibers are randomly located (i.e., not evenly spaced) in the RVE, in contrast with the hypothesis of evenly spaced fibers adopted by the micromechanical models presented in Section 5.1. Nevertheless, as depicted in Fig. 16a, the values of $E^c_{xx}$ obtained with the numerical simulations are in good agreement with those provided by the analytical micromechanical models, and especially with the Halpin-Tsai model [84]. For the sake of completeness, we generated also RVEs with equally spaced unidirectional fibers and the corresponding results (not shown here) were identical to those reported in Fig. 16a–e.

### 5.3. Random reinforcement

For the case of randomly oriented CNTs, the out of diagonal terms in the second order tensor of fibers distribution $a_{ij}$ were not identically equal to zero (see (37)) implying that the corresponding RVEs are not perfectly isotropic. By way of example, the elastic constitutive matrix for an (8,8)-polymer composite is

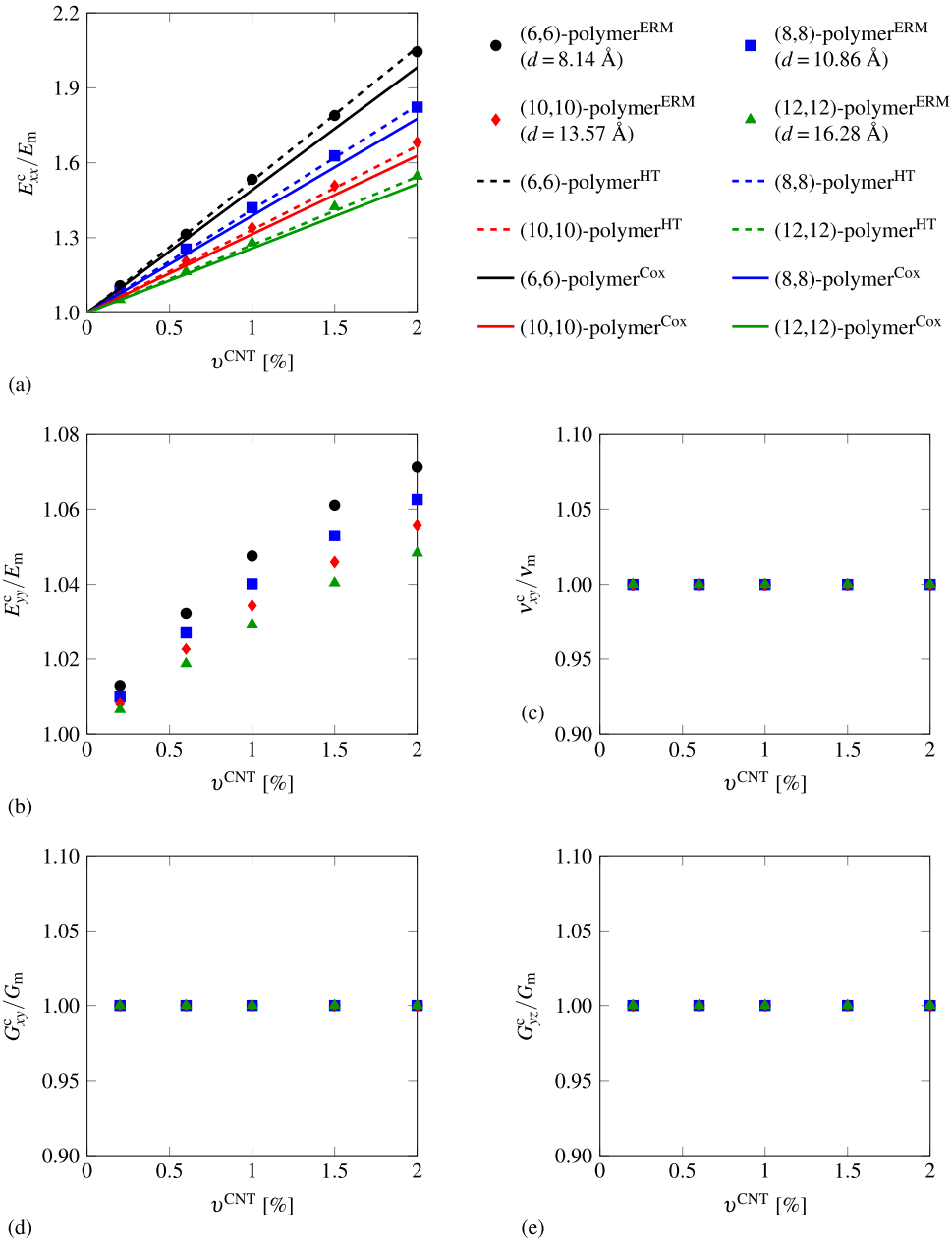


**Fig. 16.** Normalized elastic properties (a) $E^c_{xx}$, (b) $E^c_{yy}$, (c) $\nu^c_{xy}$, (d) $G^c_{xy}$ and (e) $G^c_{yz}$ for $(n,n)$-polymer composites with unidirectional CNTs. For the case of $E^c_x$, results are in good agreement with those obtained with the Halpin-Tsai (HT) and Cox micromechanical models.

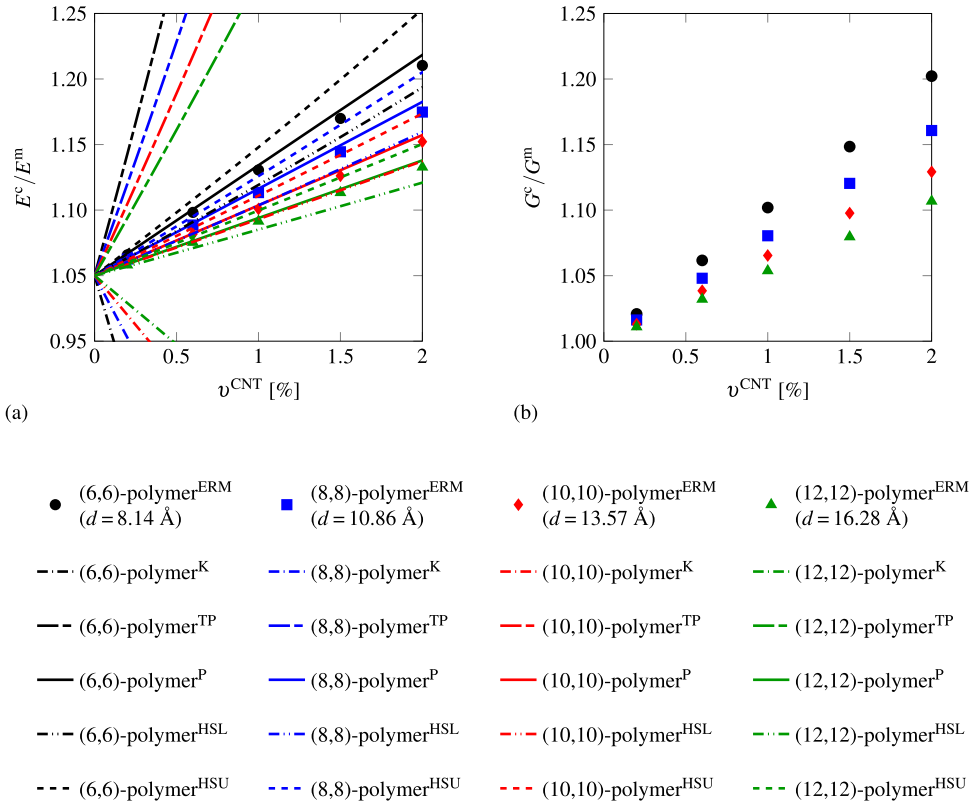


**Fig. 17.** Normalized elastic properties (a) $E^c$ and (b) $G^c$ for $(n,n)$-polymer-polymer composites with randomly oriented CNTs. Results for the Young's modulus $E^c$ of the composite are compared to those obtained with the Krenchel (K), Tsai-Pagano (TP), Pan (P) micromechanical models and the Hashin-Shtrikman upper (HSU) and lower (HSL) bounds.

$$\boldsymbol{C} = \begin{bmatrix} 5.3700 & 2.9938 & 2.9939 & 0.0015 & 0.0027 & 0.0046 \\ 2.9938 & 5.3751 & 2.9943 & 0.0012 & 0.0011 & 0.0032 \\ 2.9939 & 2.9943 & 5.3747 & 0.0013 & 0.0003 & 0.0011 \\ 0.0015 & 0.0012 & 0.0013 & 2.4121 & 0.0032 & 0.0003 \\ 0.0027 & 0.0011 & 0.0003 & 0.0032 & 2.4111 & 0.0014 \\ 0.0046 & 0.0032 & 0.0011 & 0.0003 & 0.0014 & 2.4114 \end{bmatrix}. \quad (47)$$

Nevertheless, the off-diagonal terms in the 4th, 5th and 6th rows and columns are about three orders of magnitude lower than the other entries. Moreover, since the matrix is symmetric and the diagonal entries in top-left and right-bottom blocks are close to each others, it is reasonable to assume that the RVE is isotropic. The two Lamé constants are therefore calculated as

$$\lambda^c = \frac{C^c_{12} + C^c_{13} + C^c_{23}}{3} \text{ and } \mu^c = \frac{C^c_{44} + C^c_{55} + C^c_{66}}{3}, \quad (48)$$

and the Young's modulus $E^c$ and shear modulus $G^c$ are derived from (34).

As shown in Fig. 17a–b, also for RVEs with randomly oriented CNTs, $E^c$ and $G^c$ linearly increase with $v^{CNT}$. Compared with the case where CNTs are perfectly aligned along the $x$ direction, the improvement in the elastic properties is lower while the opposite is observed for the shear modulus (similar results were derived numerically in Ref. [85]). Here, the estimated values of $E^c$ and $G^c$ provided by the Krenchel and Tsai-Pagano models are far from those obtained with FEM simulations. Surprisingly, the trend of $E^c$ obtained with the Krenchel model is the opposite of the expected one: this is a consequence of the low Young's modulus of the interphase region (for higher values the usual trend would be observed). On the contrary, the Pan model provides a good estimate. Moreover, the numerical results are within the Hashin-Shtrikman bounds.

### 5.4. Size effects

Fig. 16 shows that in unidirectional CNT-polymer composites an overall reinforcement effect is noticed decreasing the diameter of the embedded nanotubes: $E^c_{xx}$, $E^c_{yy}$, $G^c_{xy}$ and $G^c_{yz}$ decrease with $d$. The opposite trend is observed for $\nu^c_{xy}$. Similarly, in CNT-polymer composites with randomly oriented fibers (see Fig. 17), $E^c$ and $G^c$ increase by decreasing the diameter of the nanotubes. In both cases, the reinforcement effect provided by $(6,6)$ CNTs on the mechanical properties of the pure polymer matrix is typically twice of that offered by $(12,12)$ CNTs.

Therefore, as discussed in Section 3, the role played by the interphase volume fraction on the composite mechanical properties is crucial. Although the stiffness of the interphase increase with $d$ (Fig. 9), that of the corresponding composites increases by decreasing $d$ (Figs. 16 and 17).

## 6. Summary and concluding remarks

The computational procedure proposed in this work hinges on the characterization of the roles played by the various phases of a CNT-polymer composite on its mechanical response.

The atomistic simulations of a generic polymer matrix embedding an uncapped nonfunctionalized single-walled CNT in Section 2 have been fundamental for the geometrical characterization of the different phases (i.e., single-walled CNT, interface, interphase and bulk polymer) and for the definition of their roles in the mechanical

response of the composite. This task addressed a crucial issue concerning nanocomposites: the separate reinforcement effect of the CNT and the interphase [26]. The results of our simulations reveals that the reinforcement in the nonfunctionalized CNT-polymer composites is solely exerted by the interphase. Despite the simplicity and generality of the atomistic polymer model, our results are supported by literature findings on some real nonfunctionalized CNT-polymer composites obtained through experiments [11,13,15–18] and numerical simulations [7,19,22,37].

This characterization justified the intermediate micromechanical model proposed in Section 3 that, at variance with previous contributions [7,21,86–88], does not take into account the embedded CNT and the interface. The elastic properties (i.e, Young's modulus and Poisson's ratio) of the interphase were determined through a parameter identification procedure by comparing the mechanical response of the atomistic model and a mechanically equivalent intermediate continuum micromechanical model. Not surprisingly, the stiffness of the interphase increases with the CNT diameter $d$ since the ordering of the surrounding polymer layer improves with increasing values of $d$ [19,20].

Finally, the mechanical properties of the composite in Section 5 were calculated through the computational homogenization procedure described in Section 4. Different RVEs embedding one-dimensional discrete fibers, representing equivalent continuum CNT-induced interphases, have been generated. The ERM was employed to efficiently take into account the high number of fibers in the FEM simulations. The results show that the elastic properties can significantly increase when the nanotubes diameter decreases, clearly indicating size-dependent effective elastic properties.

Due to the generality of the model for the polymer chains, it is difficult, and beyond the scope of the paper, to quantitatively compare the estimated macroscopic elastic properties with literature findings on real CNT-polymer composites. Nevertheless, similarities with experimental results on composites showing CNT-nucleated crystallization can be found. For instance, Coleman and coworkers [11,12] observed that Young's modulus and crystallinity in CNT-polyvinyl alcohol linearly increase with $v_{CNT}$ as observed in the present study. Hegde et al. [18] also noticed a linear increase in the Young's modulus with the CNT diameter $d$. Moreover, some experiments on CNT-polymer composites [12,18,89] showed that the stiffness does not increase after a certain value of $v_{CNT}$. This might suggest full crystallization of the polymer matrix and supports, as discussed in Section 2.4, the relevant role of the interphase beside the negligible one of the interface for composites with non-functionalized CNTs.

## Acknowledgement

The research leading to these results has received funding from MIUR (Fondo Giovani 2011), the European Research Council under the European Union's Seventh Framework Programme (FP7/2007-2013)/ERC Grant agreement no 617972, and the National Research grant PRIN 2015 “Multi-scale mechanical models for the design and optimization of micro-structured smart materials and meta-materials” 2015LYYXA8.

## Appendix

### *A Periodic boundary conditions for three-dimensional RVE*

For the RVE in Fig. 18 with dimensions $L_x$, $L_y$ and $L_z$, the periodic boundary conditions [90] can be stated as

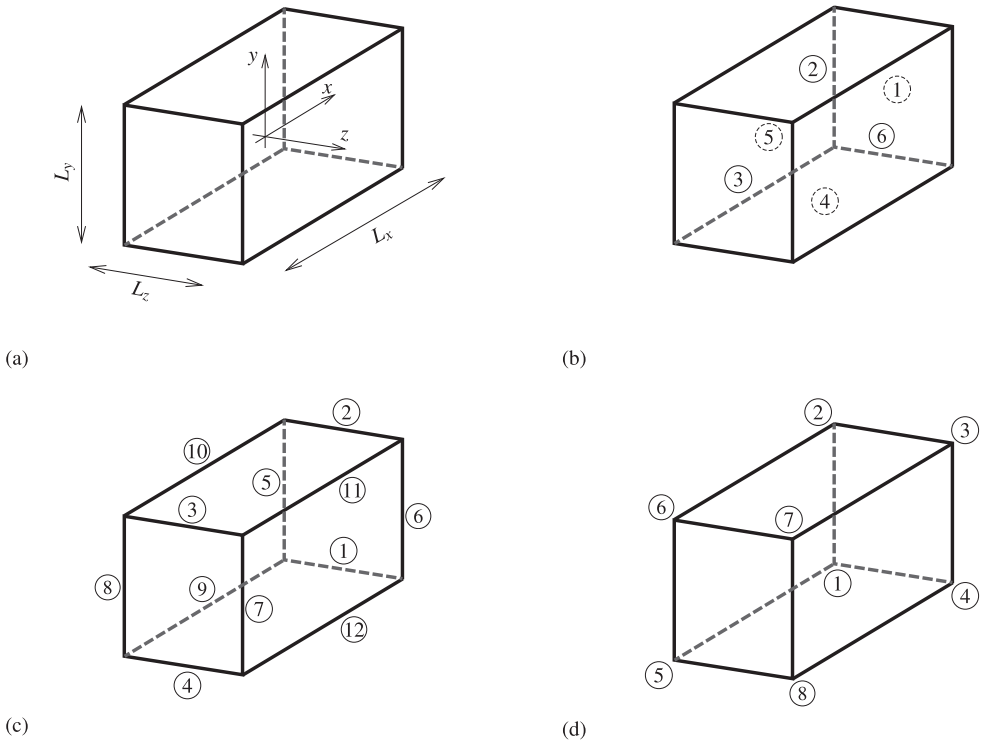


**Fig. 18.** (a) Schematic representation of a three-dimensional RVE and numbering of (b) faces, (c) edges and (d) vertices.

$$u_i^k - u_i^l = \bar{\varepsilon}_{ij} L_j \tag{49}$$

where $u_i^k$ and $u_i^l$ are the displacements in $i$-direction on the two opposite boundaries denoted by indexes $k$ and $l$ while $\bar{\varepsilon}_{ij}$ is the imposed macrostrain tensor. Therefore, with reference to Fig. 18b–d, the periodic boundary conditions for a generic macrostrain can be explicitly written for all faces:

$$u_x^1 = u_x^3 + \bar{\varepsilon}_{xx} L_x, \tag{50a}$$

$$u_y^1 = u_y^3 + \bar{\varepsilon}_{yx} L_x, \tag{50b}$$

$$u_z^1 = u_z^3 + \bar{\varepsilon}_{zx} L_x, \tag{50c}$$

$$u_x^2 = u_x^4 + \bar{\varepsilon}_{xy} L_y, \tag{51a}$$

$$u_y^2 = u_y^4 + \bar{\varepsilon}_{yy} L_y, \tag{51b}$$

$$u_z^2 = u_z^4 + \bar{\varepsilon}_{zy} L_y, \tag{51c}$$

$$u_x^6 = u_x^5 + \bar{\varepsilon}_{xz} L_z, \tag{52a}$$

$$u_y^6 = u_y^5 + \bar{\varepsilon}_{yz} L_z, \tag{52b}$$

$$u_z^6 = u_z^5 + \bar{\varepsilon}_{zz} L_z, \tag{52c}$$

edges:

$$u_x^2 = u_x^3 + \bar{\varepsilon}_{xx} L_x, \tag{53a}$$

$$u_y^2 = u_y^3 + \bar{\varepsilon}_{yx} L_x, \tag{53b}$$

$$u_z^2 = u_z^3 + \bar{\varepsilon}_{zx} L_x, \tag{53c}$$

$$u_x^3 = u_x^4 + \bar{\varepsilon}_{xy} L_y, \tag{54a}$$

$$u_y^3 = u_y^4 + \bar{\varepsilon}_{yy} L_y, \tag{54b}$$

$$u_z^3 = u_z^4 + \bar{\varepsilon}_{zy} L_y, \tag{54c}$$

$$u_x^1 = u_x^4 + \bar{\varepsilon}_{xx} L_x, \tag{55a}$$

$$u_y^1 = u_y^4 + \bar{\varepsilon}_{yx} L_x, \tag{55b}$$

$$u_z^1 = u_z^4 + \bar{\varepsilon}_{zx} L_x, \tag{55c}$$

$$u_x^6 = u_x^7 + \bar{\varepsilon}_{xx} L_x, \tag{56a}$$

$$u_y^6 = u_y^7 + \bar{\varepsilon}_{yx} L_x, \tag{56b}$$

$$u_z^6 = u_z^7 + \bar{\varepsilon}_{zx} L_x, \tag{56c}$$

$$u_x^7 = u_x^8 + \bar{\varepsilon}_{xy} L_z, \tag{57a}$$

$$u_y^7 = u_y^8 + \bar{\varepsilon}_{yy} L_z, \tag{57b}$$

$$u_z^7 = u_z^8 + \bar{\varepsilon}_{zy} L_z, \tag{57c}$$

$$u_x^5 = u_x^8 + \bar{\varepsilon}_{xx} L_x, \tag{58a}$$

$$u_y^5 = u_y^8 + \bar{\varepsilon}_{yx} L_x, \tag{58b}$$

$$u_z^5 = u_z^8 + \bar{\varepsilon}_{zx} L_x, \tag{58c}$$

$$u_x^{11} = u_x^{10} + \bar{\varepsilon}_{xz} L_z, \tag{59a}$$

$$u_y^{11} = u_y^{10} + \bar{\varepsilon}_{yz} L_z, \tag{59b}$$

$$u_z^{11} = u_z^{10} + \bar{\varepsilon}_{zz} L_z, \tag{59c}$$

$$u_x^{11} = u_x^{12} + \bar{\varepsilon}_{xy} L_y, \tag{60a}$$

$$u_y^{11} = u_y^{12} + \bar{\varepsilon}_{yy} L_y, \tag{60b}$$

$$u_z^{11} = u_z^{12} + \bar{\varepsilon}_{zy} L_y, \tag{60c}$$

$$u_x^{12} = u_x^9 + \bar{\varepsilon}_{xz} L_z, \tag{61a}$$

$$u_y^{12} = u_y^9 + \bar{\varepsilon}_{yz} L_z, \tag{61b}$$

$$u_z^{12} = u_z^9 + \bar{\varepsilon}_{zz} L_z, \tag{61c}$$

and vertices:

$$u_x^2 = u_x^1 + \bar{\varepsilon}_{xy} L_y, \tag{62a}$$

$$u_y^2 = u_y^1 \bar{\varepsilon}_{yy} L_y, \tag{62b}$$

$$u_z^2 = u_z^1 + \bar{\varepsilon}_{zy} L_y, \tag{62c}$$

$$u_x^3 = u_x^2 + \bar{\varepsilon}_{xz} L_z, \tag{63a}$$

$$u_y^3 = u_y^2 + \bar{\varepsilon}_{yz} L_z, \tag{63b}$$

$$u_z^3 = u_z^2 + \bar{\varepsilon}_{zz} L_z, \tag{63c}$$

$$u_x^3 = u_x^4 + \bar{\varepsilon}_{xy} L_y, \tag{64a}$$

$$u_y^3 = u_y^4 + \bar{\varepsilon}_{yy} L_y, \tag{64b}$$

$$u_z^3 = u_z^4 + \bar{\varepsilon}_{zy} L_y, \tag{64c}$$

$$u_x^7 = u_x^8 + \bar{\varepsilon}_{xy} L_y, \tag{65a}$$

$$u_y^7 = u_y^8 + \bar{\varepsilon}_{yy} L_y, \tag{65b}$$

$$u_z^7 = u_z^8 + \bar{\varepsilon}_{zy} L_y, \tag{65c}$$

$$u_x^7 = u_x^6 + \bar{\varepsilon}_{xz} L_z, \tag{66a}$$

$$u_y^7 = u_y^6 + \bar{\varepsilon}_{yz} L_z, \tag{66b}$$

$$u_z^7 = u_z^6 + \bar{\varepsilon}_{zz} L_z, \tag{66c}$$

$$u_x^6 = u_x^5 + \bar{\varepsilon}_{xy} L_y, \tag{67a}$$

$$u_y^6 = u_y^5 + \bar{\varepsilon}_{yy} L_y, \tag{67b}$$

$$u_z^6 = u_z^5 + \bar{\varepsilon}_{zy} L_y, \tag{67c}$$

$$u_x^4 = u_x^8 + \bar{\varepsilon}_{xx} L_x, \tag{68a}$$

$$u_y^4 = u_y^8 + \bar{\varepsilon}_{yx} L_x, \tag{68b}$$

$$u_z^4 = u_z^8 + \bar{\varepsilon}_{zx} L_x. \tag{68c}$$

If the RVE is symmetric with respect to the *xy*, *xz* and *yz* planes, displacements on opposite faces are such that

$$u_x^1 = -u_x^3, \tag{69a}$$

$$u_y^2 = -u_y^4, \quad \text{and} \tag{69b}$$

$$u_z^5 = -u_z^6. \tag{69c}$$

Substituting (69a)-(69c) in (50a), (51a) and (52a), respectively, for $\bar{\varepsilon} = [\bar{\varepsilon}_{xx} 0\ 0\ 0\ 0\ 0]^{\mathrm{T}}$ yields

$$u_x^1 = -u_x^3 = \bar{\varepsilon}_{xx} \frac{L_x}{2}, \tag{70a}$$

$$u_y^2 = u_y^4 = 0, \quad \text{and} \tag{70b}$$

$$u_z^5 = u_z^6 = 0. \tag{70c}$$

This implies that the displacements orthogonal to faces 4, 6, 2 and 5 are null. Therefore, with reference to the equivalent continuum model in discussed in Section 3, derivation of the boundary conditions in Fig. 7b is straightforward.

**Table 6**
NURBS degree and knot vectors used for the five NURBS patches in Fig. 7.

| Direction | Degree | Knot vector |
|---|---|---|
| $\xi$ | $p = 1$ | $\Xi = [0, , 1, 1]$ |
| $\eta$ | $q =$ | $\mathscr{H} = [0, 0, 0, 1, 1, 1]$ |
| $\zeta$ | $r = 1$ | $\mathscr{Z} = [0, 0, 1, 1]$ |

**Table 7**
Control points and weights for the five NURBS patches in Fig. 7.

| Patch | $j$ | $k$ | $B_{1,j,k}$ | $w_{1,j,k}$ | $B_{2,j,k}$ | $w_{2,j,k}$ |
|---|---|---|---|---|---|---|
| 1 | 1 | 1 | $(0, B, 0)$ | 1 | $(l/2, B, 0)$ | 1 |
| | 2 | 1 | $(0, B/2, B/2)$ | 1 | $(l/2, B/2, B/2)$ | 1 |
| | 3 | 1 | $(0, 0, B)$ | 1 | $(l/2, 0, B)$ | 1 |
| | 1 | 2 | $(0, r^{\mathrm{f}}, 0)$ | 1 | $(l/2, r^{\mathrm{f}}, 0)$ | 1 |
| | 2 | 2 | $(0, r^{\mathrm{f}}\cos\pi/4, r^{\mathrm{f}}\sin\pi/4)$ | $1/\sqrt{2}$ | $(l/2\sqrt{2}, r^{\mathrm{f}}\cos\pi/4, r^{\mathrm{f}}\sin\pi/4)$ | $1/\sqrt{2}$ |
| | 3 | 2 | $(0, 0, r^{\mathrm{f}})$ | 1 | $(l/2, 0, r^{\mathrm{f}})$ | 1 |
| 2 | 1 | 1 | $(0, r^{\mathrm{f}}, 0)$ | 1 | $(l/2, r^{\mathrm{f}}, 0)$ | 1 |
| | 2 | 1 | $(0, r^{\mathrm{f}}\cos\pi/4, r^{\mathrm{f}}\sin\pi/4)$ | $1/\sqrt{2}$ | $(l/2\sqrt{2}, r^{\mathrm{f}}\cos\pi/4, r^{\mathrm{f}}\sin\pi/4)$ | $1/\sqrt{2}$ |
| | 3 | 1 | $(0, 0, r^{\mathrm{f}})$ | 1 | $(l/2, 0, r^{\mathrm{f}})$ | 1 |
| | 1 | 2 | $(0, r^{\mathrm{i}}, 0)$ | 1 | $(l/2, r^{\mathrm{i}}, 0)$ | 1 |
| | 2 | 2 | $(0, r^{\mathrm{i}}\cos\pi/4, r^{\mathrm{i}}\sin\pi/4)$ | $1/\sqrt{2}$ | $(l/2\sqrt{2}, r^{\mathrm{i}}\cos\pi/4, r^{\mathrm{i}}\sin\pi/4)$ | $1/\sqrt{2}$ |
| | 3 | 2 | $(0, 0, r^{\mathrm{i}})$ | 1 | $(l/2, 0, r^{\mathrm{i}})$ | 1 |
| 3 | 1 | 1 | $(l/2, B, 0)$ | 1 | $(L_x/2, B, 0)$ | 1 |
| | 2 | 1 | $(l/2, B/2, B/2)$ | 1 | $(L_x/2, B/2, B/2)$ | 1 |
| | 3 | 1 | $(l/2, 0, B)$ | 1 | $(L_x/2, 0, B)$ | 1 |
| | 1 | 2 | $(l/2, r^{\mathrm{f}}, 0)$ | 1 | $(L_x/2, r^{\mathrm{f}}, 0)$ | 1 |
| | 2 | 2 | $(l/2\sqrt{2}, r^{\mathrm{f}}\cos\pi/4, r^{\mathrm{f}}\sin\pi/4)$ | $1/\sqrt{2}$ | $(L_x/2\sqrt{2}, r^{\mathrm{f}}\cos\pi/4, r^{\mathrm{f}}\sin\pi/4)$ | $1/\sqrt{2}$ |
| | 3 | 2 | $(l/2, 0, r^{\mathrm{f}})$ | 1 | $(L_x/2, 0, r^{\mathrm{f}})$ | 1 |
| 4 | 1 | 1 | $(l/2, r^{\mathrm{i}}, 0)$ | 1 | $(L_x/2, r^{\mathrm{i}}, 0)$ | 1 |
| | 2 | 1 | $(l/2\sqrt{2}, r^{\mathrm{i}}\cos\pi/4, r^{\mathrm{i}}\sin\pi/4)$ | $1/\sqrt{2}$ | $(L_x/2\sqrt{2}, r^{\mathrm{i}}\cos\pi/4, r^{\mathrm{i}}\sin\pi/4)$ | $1/\sqrt{2}$ |
| | 3 | 1 | $(l/2, 0, r^{\mathrm{i}})$ | 1 | $(L_x/2, 0, r^{\mathrm{i}})$ | 1 |
| | 1 | 2 | $(l/2, r^{\mathrm{f}}, 0)$ | 1 | $(L_x/2, r^{\mathrm{f}}, 0)$ | 1 |
| | 2 | 2 | $(l/2\sqrt{2}, r^{\mathrm{f}}\cos\pi/4, r^{\mathrm{f}}\sin\pi/4)$ | $1/\sqrt{2}$ | $(L_x/2\sqrt{2}, r^{\mathrm{f}}\cos\pi/4, r^{\mathrm{f}}\sin\pi/4)$ | $1/\sqrt{2}$ |
| | 3 | 2 | $(l/2, 0, r^{\mathrm{f}})$ | 1 | $(L_x/2, 0, r^{\mathrm{f}})$ | 1 |
| 5 | 1 | 1 | $(l/2, 0, 0)$ | 1 | $(L_x/2, 0, 0)$ | 1 |
| | 2 | 1 | $(l/2\sqrt{2}, 0, 0)$ | $1/\sqrt{2}$ | $(L_x/2\sqrt{2}, 0, 0)$ | $1/\sqrt{2}$ |
| | 3 | 1 | $(l/2, 0, 0)$ | 1 | $(L_x/2, 0, 0)$ | 1 |
| | 1 | 2 | $(l/2, r^{\mathrm{i}}, 0)$ | 1 | $(L_x/2, r^{\mathrm{i}}, 0)$ | 1 |
| | 2 | 2 | $(l/2, r^{\mathrm{i}}\cos\pi/4, r^{\mathrm{i}}\sin\pi/4)$ | $1/\sqrt{2}$ | $(L_x/2\sqrt{2}, r^{\mathrm{i}}\cos\pi/4, r^{\mathrm{i}}\sin\pi/4)$ | $1/\sqrt{2}$ |
| | 3 | 2 | $(l/2, 0, 0)$ | 1 | $(L_x/2, 0, 0)$ | 1 |

### *B Control data for the NURBS continuum equivalent model*

The knot vectors and control points required for the multi-patch NURBS solid shown in Fig. 7 are reported in Tables 6 and 7, respectively.

## References


[1] Barber AH, Cohen SR, Wagner HD. Measurement of carbon nanotube–polymer interfacial strength. Appl Phys Lett 2003;82(23):4140–2.

[2] Barber AH, Cohen SR, Kenig S, Wagner HD. Interfacial fracture energy measurements for multi-walled carbon nanotubes pulled from a polymer matrix. Compos Sci Technol 2004;64(15):2283–9.

[3] Li Y, Liu Y, Peng X, Yan C, Liu S, Hu N. Pull-out simulations on interfacial properties of carbon nanotube-reinforced polymer nanocomposites. Comput Mater Sci 2011;50(6):1854–60.

[4] Zhang ZQ, Ward DK, Xue Y, Zhang HW, Horstemeyer MF. Interfacial characteristics of carbon nanotube-polyethylene composites using molecular dynamics simulations. ISRN Mater Sci 2011:2011.

[5] Coto B, Antia I, Barriga J, Blanco M, Sarasua J-S. Influence of the geometrical properties of the carbon nanotubes on the interfacial behavior of epoxy/CNT composites: a molecular modelling approach. Comput Mater Sci 2013;79:99–104.

[6] Chen X, Zhang L, Zheng M, Park C, Wang X, Ke C. Quantitative nanomechanical characterization of the van der waals interfaces between carbon nanotubes and epoxy. Carbon 2015;82:214–28.

[7] Choi J, Shin H, Cho M. A multiscale mechanical model for the effective interphase of SWNT/epoxy nanocomposite. Polymer 2016;89:159–71.

[8] Wernik JM, Cornwell-Mott BJ, Meguid SA. Determination of the interfacial properties of carbon nanotube reinforced polymer composites using atomistic-based continuum model. Int J Solids Struct 2012;49(13):1852–63.

[9] Laird ED, Li CY. Structure and morphology control in crystalline polymer–carbon nanotube nanocomposites. Macromolecules 2013;46(8):2877–91.
[10] Karatrantos A, Clarke N, Kröger M. Modeling of polymer structure and conformations in polymer nanocomposites from atomistic to mesoscale: a review. Polym Rev 2016;56(3):385–428.
[11] Coleman JN, Cadek M, Ryan KP, Fonseca A, Nagy JB, Blau WJ, et al. Reinforcement of polymers with carbon nanotubes. The role of an ordered polymer interfacial region. Experiment and modeling. Polymer 2006;47(26):8556–61.
[12] Ryan KP, Cadek M, Nicolosi V, Blond D, Ruether M, Armstrong G, et al. Carbon nanotubes for reinforcement of plastics? A case study with poly (vinyl alcohol). Compos Sci Technol 2007;67(7):1640–9.
[13] Schadler LS, Giannaris SC, Ajayan PM. Load transfer in carbon nanotube epoxy composites. Appl Phys Lett 1998;73(26):3842–4.
[14] Ajayan PM, Schadler LS, Giannaris C, Rubio A. Single-walled carbon nanotube–polymer composites: strength and weakness. Adv Mater 2000;12(10):750–3.
[15] Watts PCP, Hsu WK. Behaviours of embedded carbon nanotubes during film cracking. Nanotechnology 2003;14(5):L7.
[16] Wang S, Liang R, Wang B, Zhang C. Load-transfer in functionalized carbon nanotubes/polymer composites. Chem Phys Lett 2008;457(4):371–5.
[17] Fragneaud B, Masenelli-Varlot K, Gonzalez-Montiel A, Terrones M, Cavaillé J-Y. Mechanical behavior of polystyrene grafted carbon nanotubes/polystyrene nanocomposites. Compos Sci Technol 2008;68(15):3265–71.
[18] Hegde M, Lafont U, Norder B, Picken SJ, Samulski ET, Rubinstein M, et al. SWCNT induced crystallization in an amorphous all-aromatic poly(ether imide). Macromolecules 2013;46(4):1492–503.
[19] Falkovich SG, Larin SV, Lyulin AV, Yudin VE, Kenny JM, Lyulin SV. Influence of the carbon nanofiller surface curvature on the initiation of crystallization in thermoplastic polymers. RSC Adv 2014;4(89):48606–12.
[20] Malagù M, Lyulin A, Benvenuti E, Simone A. A molecular-dynamics study of size and chirality effects on glass-transition temperature and ordering in carbon nanotube-polymer composites. Macromol Theory Simulations 2016;25(6):571–81.
[21] Odegard GM, Gates TS, Wise KE, Park C, Siochi EJ. Constitutive modeling of nanotube–reinforced polymer composites. Compos Sci Technol 2003;63(11):1671–87.
[22] Yang S, Yu S, Kyoung W, Hanand D-S, Cho M. Multiscale modeling of size-dependent elastic properties of carbon nanotube/polymer nanocomposites with interfacial imperfections. Polymer 2012;53(2):623–33.
[23] Yang S, Yu S, Ryu J, Cho J-M, Kyoung W, Han D-S, et al. Nonlinear multiscale modeling approach to characterize elastoplastic behavior of cnt/polymer nanocomposites considering the interphase and interfacial imperfection. Int J Plasticity 2013;41:124–46.
[24] Choi J, Shin H, Yang S, Cho M. The influence of nanoparticle size on the mechanical properties of polymer nanocomposites and the associated interphase region: a multiscale approach. Compos Struct 2015;119:365–76.
[25] Phillips DV, Zienkiewicz OC. Finite element non-linear analysis of concrete structures. Proc Institution Civ Eng Part 2 1976;61:59–88.
[26] Pukánszky B. Interfaces and interphases in multicomponent materials: past, present, future. Eur Polym J 2005;41(4):645–62.
[27] Weidt D, Figiel Ł. Effect of CNT waviness and van der Waals interaction on the nonlinear compressive behaviour of epoxy/CNT nanocomposites. Compos Sci Technol 2015;115:52–9.
[28] Dresselhaus MS, Dresselhaus G, Eklund PC, Rao AM. Carbon nanotubes. Springer; 2000.
[29] Belytschko T, Xiao SP, Schatz GC, Ruoff RS. Atomistic simulations of nanotube fracture. Phys Rev B 2002;65(23):235430.
[30] Tserpes KI, Papanikos P, Labeas G, Pantelakis SG. Multi-scale modeling of tensile behavior of carbon nanotube-reinforced composites. Theor Appl Fract Mech 2008;49(1):51–60.
[31] Malagù M, Benvenuti E, Simone A. One-dimensional nonlocal elasticity for tensile single-walled carbon nanotubes: a molecular structural mechanics characterization. Eur J Mechanics-A/Solids 2015;54:160–70.
[32] Kremer K, Grest GS. Dynamics of entangled linear polymer melts: a molecular-dynamics simulation. J Chem Phys 1990;92(8):5057–86.
[33] Karatrantos A, Composto RJ, Winey KI, Clarke N. Structure and conformations of polymer/SWCNT nanocomposites. Macromolecules 2011;44(24):9830–8.
[34] Liew KM, He XQ, Wong CH. On the study of elastic and plastic properties of multi-walled carbon nanotubes under axial tension using molecular dynamics simulation. Acta Mater 2004;52(9):2521–7.
[35] Brenner DW. Empirical potential for hydrocarbons for use in simulating the chemical vapor deposition of diamond films. Phys Rev B 1990;42(15):9458.
[36] Theodorou DN, Suter UW. Detailed molecular structure of a vinyl polymer glass. Macromolecules 1985;18(7):1467–78.
[37] Herasati S, Zhang LC, Ruan HH. A new method for characterizing the interphase regions of carbon nanotube composites. Int J Solids Struct 2014;51(9):1781–91.
[38] Plimpton S. Fast parallel algorithms for short-range molecular dynamics. J Comput Phys 1995;117(1):1–19.
[39] Pipes RB, Frankland SJV, Hubert P, Saether E. Self-consistent properties of carbon nanotubes and hexagonal arrays as composite reinforcements. Compos Sci Technol 2003;63(10):1349–58.
[40] Frankland SJV, Harik VM, Odegard GM, Brenner DW, Gates TS. The stress-strain behavior of polymer-nanotube composites from molecular dynamics simulation. Compos Sci Technol 2003;63(11):1655–61.
[41] Han Y, Elliott J. Molecular dynamics simulations of the elastic properties of polymer/carbon nanotube composites. Comput Mater Sci 2007;39(2):315–23.
[42] Zhu R, Pan E, Roy AK. Molecular dynamics study of the stress-strain behavior of carbon-nanotube reinforced Epon 862 composites. Mater Sci Eng A 2007;447(1):51–7.
[43] Huang Y, Wu J, Hwang K-C. Thickness of graphene and single-wall carbon nanotubes. Phys Rev B 2006;74(24):245413.
[44] Werder T, Walther JH, Jaffe RL, Halicioglu T, Koumoutsakos P. On the water-carbon interaction for use in molecular dynamics simulations of graphite and carbon nanotubes. J Phys Chem B 2003;107(6):1345–52.
[45] Clancy TC, Gates TS. Modeling of interfacial modification effects on thermal conductivity of carbon nanotube composites. Polymer 2006;47(16):5990–6.
[46] Haghighatpanah S, Bolton K. Molecular-level computational studies of single wall carbon nanotube–polyethylene composites. Comput Mater Sci 2013;69:443–54.
[47] Larin SV, Falkovich SG, Nazarychev VM, Gurtovenko AA, Lyulin AV, Lyulin SV. Molecular-dynamics simulation of polyimide matrix pre-crystallization near the surface of a single-walled carbon nanotube. RSC Adv 2014;4(2):830–44.
[48] Brown D, Marcadon V, Mele P, Alberola ND. Effect of filler particle size on the properties of model nanocomposites. Macromolecules 2008;41(4):1499–511.
[49] Hadden CM, Jensen BD, Bandyopadhyay A, Odegard GM, Koo A, Liang R. Molecular modeling of EPON-862/graphite composites: interfacial characteristics for multiple crosslink densities. Compos Sci Technol 2013;76:92–9.
[50] Mokashi VV, Qian D, Liu Y. A study on the tensile response and fracture in carbon nanotube-based composites using molecular mechanics. Compos Sci Technol 2007;67(3):530–40.
[51] Arash B, Wang Q, Varadan VK. Mechanical properties of carbon nanotube/polymer composites. Sci Rep 2014;4.
[52] Lan M, Waisman H. Mechanics of SWCNT aggregates studied by incremental constrained minimization. J Nanomechanics Micromechanics 2011;2(2):15–22.
[53] Qian D, Dickey EC, Andrews R, Rantell T. Load transfer and deformation mechanisms in carbon nanotube-polystyrene composites. Appl Phys Lett 2000;76(20):2868–70.
[54] Qian D, Dickey EC. In-situ transmission electron microscopy studies of polymer-carbon nanotube composite deformation. J Microsc 2001;204(1):39–45.
[55] Cooper CA, Cohen S, Barber AH, Wagner HD. Detachment of nanotubes from a polymer matrix. Appl Phys Lett 2002;81(20):3873–5.
[56] Milton GW. The theory of composites. 2002. The Theory of Composites.
[57] Bower DI. An introduction to polymer physics. Cambridge University Press; 2002.
[58] Nocedal J, Wright SJ. Numerical optimization. Springer; 2006.
[59] Hughes TJR, Cottrell JA, Bazilevs Y. Isogeometric analysis: CAD, finite elements, NURBS, exact geometry and mesh refinement. Comput Methods Appl Mech Eng 2005;194(39):4135–95.
[60] De Falco C, Reali A, Vázquez R. GeoPDEs: a research tool for isogeometric analysis of PDEs. Adv Eng Softw 2011;42(12):1020–34.
[61] Cunha VMCF, Barros JAO, Sena-Cruz JM. A finite element model with discrete embedded elements for fibre reinforced composites. Comput Struct 2012;94:22–33.
[62] Balakrishnan S, Murray DW. Finite element prediction of reinforced concrete behavior. Technical Report No. 138 (Structural Engineering). Department of Civil Engineering, The University of Alberta; July 1986.
[63] Elwi AE, Hrudey TM. Finite element model for curved embedded reinforcement. J Eng Mech 1989;115(4):740–54.
[64] Halpin Affdl JC, Kardos JL. The Halpin-Tsai equations: a review. Polym Eng Sci 1976;16(5):344–52.
[65] Widom B. Random sequential addition of hard spheres to a volume. J Chem Phys 1966;44(10):3888–94.
[66] Kari S, Berger H, Gabbert U. Numerical evaluation of effective material properties of randomly distributed short cylindrical fibre composites. Comput Mater Sci 2007;39(1):198–204.
[67] Böhm HJ, Eckschlager A, Han W. Multi-inclusion unit cell models for metal matrix composites with randomly oriented discontinuous reinforcements. Comput Mater Sci 2002;25(1):42–53.
[68] Advani SG, Tucker III CL. The use of tensors to describe and predict fiber orientation in short fiber composites. J Rheology 1987;31(8):751–84.
[69] Lee Y, Lee S, Youn J, Chung K, Kang T. Characterization of fiber orientation in short fiber reinforced composites with an image processing technique. Mater Res Innovations 2002;6(2):65–72.
[70] Hill R. Elastic properties of reinforced solids: some theoretical principles. J Mech Phys Solids 1963;11(5):357–72.
[71] Hashin Z. Analysis of composite materialsa survey. J Appl Mech 1983;50(3):481–505.
[72] Ostoja-Starzewski M. Microstructural randomness versus representative volume element in thermomechanics. J Appl Mech 2002;69(1):25–35.
[73] Kanit T, Forest S, Galliet I, Mounoury V, Jeulin D. Determination of the size of the representative volume element for random composites: statistical and numerical approach. Int J Solids Struct 2003;40(13):3647–79.
[74] Tian W, Qi L, Zhou J, Liang J, Ma Y. Representative volume element for composites reinforced by spatially randomly distributed discontinuous fibers and its applications. Compos Struct 2015;131:366–73.
[75] Tucker III CL, Liang E. Stiffness predictions for unidirectional short-fiber

composites: review and evaluation. Compos Sci Technol 1999;59(5):655–71.
[76] Cox HL. The elasticity and strength of paper and other fibrous materials. Br J Appl Phys 1952;3(3):72–9.
[77] Krenchel H. Fibre reinforcement—theoretical and practical investigations of the elasticity and strength of fibre-reinforced materials (thesis). Copenhagen: Akademisk Forlag; 1964.
[78] Tsai SW, Pagano NJ. Invariant properties of composite materials. In: Tsai SW, Halpin JC, Pagano NJ, editors. Composite materials workshop. Westport: Technomic Publishing Co.; 1968. p. 233–53.
[79] Singh S, Mohanty AK. Wood fiber reinforced bacterial bioplastic composites: fabrication and performance evaluation. Compos Sci Technol 2007;67(9):1753–63.
[80] Pan N. The elastic constants of randomly oriented fiber composites: a new approach to prediction. Sci Eng Compos Mater 1996;5(2):63–72.
[81] Hashin Z, Shtrikman S. On some variational principles in anisotropic and nonhomogeneous elasticity. J Mech Phys Solids 1962;10(4):335–42.
[82] Atkinson C. Some ribbon-like inclusion problems. Int J Eng Sci 1973;11(2):243–66.
[83] Noselli G, Dal Corso F, Bigoni D. The stress intensity near a stiffener disclosed by photoelasticity. Int J Fract 2010;166(1):91–103.
[84] Gusev AA, Hine PJ, Ward IM. Fiber packing and elastic properties of a transversely random unidirectional glass/epoxy composite. Compos Sci Technol 2000;60(4):535–41.
[85] Tian W, Qi L, Su C, Zhou J, Jing Z. Numerical simulation on elastic properties of short-fiber-reinforced metal matrix composites: effect of fiber orientation. Compos Struct 2016;152:408–17.
[86] Wan H, Delale F, Shen L. Effect of CNT length and CNT-matrix interphase in carbon nanotube (CNT) reinforced composites. Mech Res Commun 2005;32(5):481–9.
[87] Liu YJ, Nishimura N, Qian D, Adachi N, Otani Y, Mokashi V. A boundary element method for the analysis of CNT/polymer composites with a cohesive interface model based on molecular dynamics. Eng Analysis Bound Elem 2008;32(4):299–308.
[88] Shokrieh MM, Rafiee R. Investigation of nanotube length effect on the reinforcement efficiency in carbon nanotube based composites. Compos Struct 2010;92(10):2415–20.
[89] Chang TE, Jensen LR, Kisliuk A, Pipes RB, Pyrz R, Sokolov AP. Microscopic mechanism of reinforcement in single-wall carbon nanotube/polypropylene nanocomposite. Polymer 2005;46(2):439–44.
[90] Sanchez-Palencia E, Zaou A. Homogenization techniques for composite media. Springer-Verlag; 1987.